

Abstract

The ultra-cryogenic gravitational wave detector NAUTILUS has taken data in Frascati (Rome), in its second science run from June 1998 to March 2002. The measured strain sensitivity at the two resonances was $4 \cdot 10^{-22} \text{ Hz}^{-1/2}$ over a bandwidth of 1 Hz. The result of the coincidence analysis with the detector EXPLORER in the year 2001 and the discovery of a potential source in the Large Magellanic Cloud (a faint optical pulsar remnant of the supernova SN1987A) set new sensitivity requirements. During 2002 the detector's read-out chain has been upgraded. We present here the work done on the electronic part of the read-out and the preliminary results of NAUTILUS 2003.

Detectors of spherical shape are being developed in Brasil and Holland. Their potentialities have not been fully exploited yet. The work of this thesis aims at approaching the final configuration of a complete detector.

One of the main limitations on the sensitivity of the operating resonant gravitational wave detectors, both cylindrical and spherical, is the noise of the first stage amplifier. A two-stage dc SQUID amplifier is being realized for the resonant gravitational wave detectors of the Rome group, in order to increase their sensitivity. The SQUID will be coupled to a high- Q electrical resonator, used as simulator of the real detector,

in order to characterize and solve most of the problems arising in these particular systems.

Contents

1	Introduction	4
1.1	Gravitational Waves	5
1.2	Gravitational Waves Detectors	7
1.2.1	Interferometric Detectors	9
1.2.2	Resonant Mass Detectors	12
2	Resonant Mass Detectors	21
2.1	On the sensitivity of a bar detector	21
2.1.1	The motion sensor	22
2.1.2	Noise	25
2.1.3	SNR	28
2.2	A brief history of bar detectors	35
2.3	The ROG detectors	39
3	The read-out of NAUTILUS	43
3.1	Influence of the electronic components on the sensitivity to bursts	49

3.2	The superconducting transformer	53
3.3	The electronic box	60
3.4	SQUID measurements	65
3.5	Preliminary results of NAUTILUS 2003	67
4	The d.c. SQUID	74
4.1	The Josephson junction	74
4.2	RSJ model	79
4.3	The d.c. SQUID	83
4.4	The SQUID as an amplifier	88
5	The read-out of MiniGRAIL	91
5.1	Noise measurement with a PZT transducer	93
5.1.1	The equivalent circuit	93
5.1.2	Noise sources of the system	95
5.1.3	Measurement of T_e	98
5.2	The MiniGRAIL electronic box	102
5.3	Measurements with single and double SQUID systems . .	104
6	Double SQUID system for the Rome detectors	106
6.1	First closed loop operation	108
6.2	Characterization of the high- Q input circuit	111
7	Conclusion	114
A	A Matlab[®] code example	116

Chapter 1

Introduction

Gravitational waves are predicted by Einstein's General Relativity. According to the same theory, gravitational waves are supposed to propagate at the speed of light and they represent a time-dependent distortion of the local space-time. Analogous in many ways to electromagnetic waves, gravitational waves are produced by the acceleration of masses, but while only a single charge is needed to produce electromagnetic waves, at least two masses are required for gravitational waves. Due to the low value of the coupling constant of the gravitational field, as Einstein himself stated, it is impossible to produce detectable gravitational waves in a laboratory. So, only astronomical scale events, such as supernovae, merging of binary systems or spinning neutron stars, are supposed to emit gravitational waves with a detectable amplitude. Direct detection of gravitational waves from astrophysical sources will fund

a new kind of astronomy. At present, the most sensitive antennas, such as the INFN NAUTILUS detector, are capable of recording only events occurring within our Galaxy. To stretch the frontier, for instance, to the Virgo Cluster, the energy resolution of the detectors must be improved by 6 orders of magnitude.

1.1 Gravitational Waves

In this section we will give a brief overview on gravitational waves within the frame of the General Relativity. Starting from the Einstein equation in vacuum

$$R_{ik} = 0 \tag{1.1}$$

and solving it in the weak field approximation, $g_{ik} = g_{ik}^0 + h_{ik}$, where g_{ik}^0 is the Minkowsky space, one finds that the solution satisfies the waves equation [1] $h_{ik,l}^l = 0$. As the gravitational field is transverse and traceless, then the only non-zero components of the of the wave field are $h_{22} = h_{33}$ and $h_{23} = -h_{32}$ (if the wave is supposed to propagate in the \mathbf{z} direction). So the field has only two polarization states. Then we can define two polarization amplitudes and write them in the plane waves format:

$$\begin{aligned} h_+ &= A_+ e^{i(\omega t - kx)} \\ h_\times &= A_\times e^{i(\omega t - kx)} \end{aligned} \tag{1.2}$$

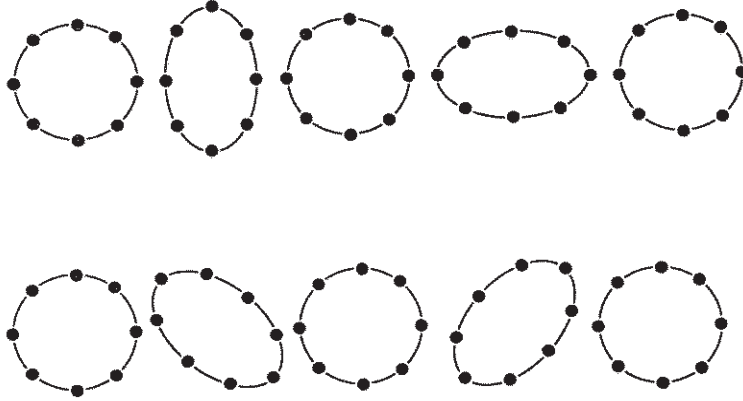


Figure 1.1: Distortion of a ring of test particles under the effect of the polarizations h_+ (upper figure) e h_x (lower figure).

The two polarization states only differ for a $\frac{\pi}{4}$ rotation about the propagation axis as shown in figure (1.1).

Astrophysical sources of gravitational waves [2], [3] can be grouped into three classes: bursts, continuous and stochastic waves. Gravitational waves bursts are high energy emissions lasting a very short time, of the order of a few milliseconds. This kind of sources includes: collapsing star into a neutron star or a black hole, coalescence of compact binary systems, supernovae explosions. The non-spherically symmetric collapse of a star of $M = 6M_\odot$ at the centre of our Galaxy would produce waves with a relative amplitude on Earth of $h_0 \sim 3 \cdot 10^{-17}$ [4]. But the rate of these events is a few over a century. If we consider a bigger volume, as big as to include the Virgo Cluster, the rate would grow to 1 event/week, but the strenght of the waves would decrease to $h_0 \sim 1.4 \cdot 10^{-20}$ [4]. Continuous

waves differ from bursts, because they last longer but the energy emitted is order of magnitude smaller. Typical sources of continuous waves are rotating compact objects or binary systems, e.g. the pulsar PSR 0532, in the Crab Nebula, would emit gravitational waves with an amplitude of the order of $h_0 \sim 10^{-26}$ [4]. The stochastic background can have two origins: as a relic of the time when the gravitons decoupled from matter (analogous to the CMB); a pop-corn like signal due to the superposition of the radiation emitted by a large population of collapsing objects in all the galaxies. The spectrum of primordial stochastic background extends through the entire frequency range [2], from $f \sim 10^{-18}$ Hz to $f \sim 1 - 10^4$ Hz and beyond. Constraints on the amplitude of this background come from Nucleosynthesis and the CMB anisotropy. See Table (1.1) for details.

1.2 Gravitational Waves Detectors

Gravitational waves antennas can be divided into two groups: resonant mass detectors and interferometers. To the first group belong both the cylindrical bars (ALLEGRO at LSU [5], AURIGA at LNL [6], EXPLORER at CERN [7] and NAUTILUS at LNF [8]) and the spheres, MiniGRAIL [9] in Holland and Mario Shenberg [10] in Brasil. While the interferometric detectors presently in operation are LIGO [11] in the US, VIRGO [12] in Italy, GEO600 [13] in Germany and TAMA300 [14] in Japan. In this section we will give a brief overlook on both resonant mass and interferometric detectors, focusing our attention on the NAUTILUS

Table 1.1: Sources of gravitational waves.

Table 1		
<u>Frequency</u>	<u>Sources</u>	<u>Detection method</u>
10^{-16} Hz	Primordial	Anisotropy of Cosmic microwave Background Radiation
10^{-9} Hz	Primordial Cosmic Strings	Timing of millisecond pulsars
10^{-4} to 10^{-1} Hz	Binary stars Supermassive BH(10^3 - $10^7 M_{\odot}$)	Doppler tracking of Spacecraft Laser interferometers in Space
$10 - 10^3$ Hz	Inspiral of NS& BH binaries($1 - 10^3 M_{\odot}$)	Laser interferometers on Earth
10^3 Hz	Coalescence of NS & BH binaries Supernovae	Resonant-mass detectors

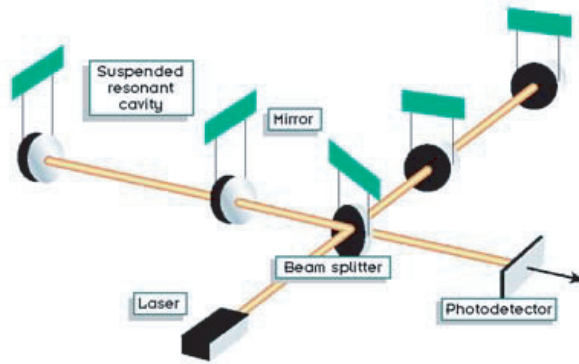


Figure 1.2: A schematic diagram of a laser interferometer gravitational wave detector.

GW Antenna.

1.2.1 Interferometric Detectors

The basic idea behind this kind of GW detector is the Michelson interferometer. A laser interferometer gravitational detector consists of four masses that hang from vibration-isolated supports as shown in figure (1.2), and the indicated optical system for monitoring the separation between the masses. Two masses are close to each other, at the corner of an “L”, and one mass is at the end of each of L’s long arms. The arms lengths are nearly equal, $L_1 \approx L_2 = L$. When a gravitational wave, with frequencies higher than the masses’ pendulum frequency (≈ 1 Hz), passes through the detector, it pushes the masses back and forth relative to each other as though they were free from their suspension wires, thereby changing the arm-length difference, $\Delta L \equiv L_1 - L_2$. That change

is monitored by laser interferometry in such a way that the variations in the output of the photodiode (the interferometers output) are directly proportional to $\Delta L(t)$.

The interferometer's output is a linear combination of the two wave fields h_+ and h_\times :

$$\frac{\Delta L(t)}{L} = F_+ h_+ + F_\times h_\times \equiv h(t) \quad (1.3)$$

The coefficients F_+ and F_\times are of the order of unity and depend in a quadrupolar manner on the direction to the source and the orientation of the detector [15].

Test masses are made of transparent fused silica, though other materials might be used in the future. The masses' inner face are covered with high-reflectivity dielectric coating to fit the mirror requirements, while the masses outer faces are covered with anti-reflection coatings. The two mirrors facing each other on each arm form a Fabry-Perot cavity. A beam splitter splits a carefully prepared laser beam in two, and directs the resulting beams down the two arms. Each beam penetrates through the antireflection coating of its arm's corner mass, through the mass, and through the dielectric coating (the mirror); and thereby - with the length of the arm's Fabry-Perot cavity adjusted to be nearly an integral number of half wavelengths of light - the beam gets trapped in the cavity. The cavity's end mirror has much higher reflectivity than its corner mirror, so the trapped light leaks back out through the corner mirror, and then

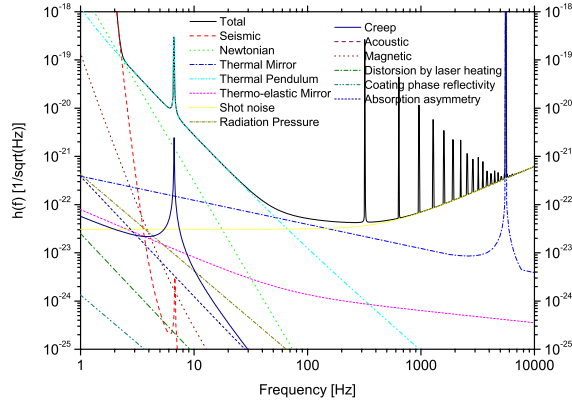


Figure 1.3: The predicted sensitivity curve for the VIRGO interferometer.

hits the beam splitter where it recombines with light from the other arm. Most of the recombined light would go back toward the laser but it is returned to the interferometer by a “light-recycling mirror”, so that the output of the interferometer is kept on the dark fringe.

When a gravitational wave hits the detector and moves the masses, thereby changing the lengths L_1 and L_2 of the two cavities, it shifts each cavity’s resonant frequency slightly relative to the laser frequency, and thereby changes the phase of the light in the cavity and the phase of the light that exits from the cavity toward the beam splitter. Correspondingly, the relative phase of the two beams returning to the splitter is altered by an amount $\Delta\Phi \propto \Delta L$, and this relative phase shift causes a change in the intensity of the recombined light at the photodiode, $\Delta I_{pd} \propto \Delta\Phi \propto \Delta L \propto h(t)$. Thus, the change of photodiode output cur-

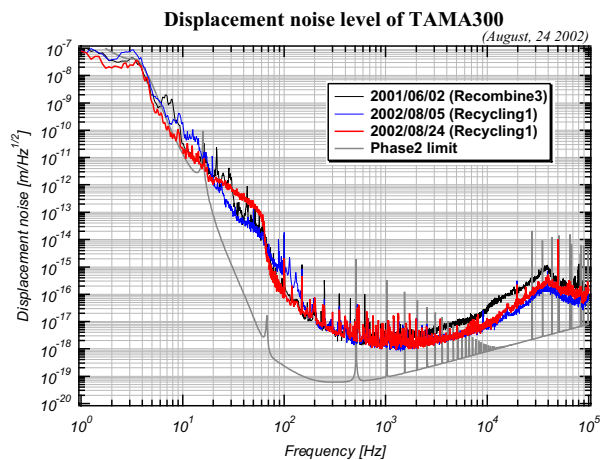


Figure 1.4: The TAMA 300 actual displacement noise level compared to the goal level.

rent is directly proportional to the gravitational-wave strain $h(t)$. This method of monitoring $h(t)$ is capable of very high sensitivity.

1.2.2 Resonant Mass Detectors

Resonant-mass antennas for gravitational radiation were pioneered by Joseph Weber about 40 years ago [16], and have been pushed to ever higher sensitivity by Weber and a number of other research groups since then. At present there is a network of such antennas [17], operating with a noise level for broad-band gravity-waves bursts of $h \simeq 6 \times 10^{-19}$.

A resonant-mass antenna consists of a solid body that (heuristically speaking) rings like a bell when a gravitational wave hits it. This body is usually a cylinder, but at least two spheres are being built [9] [10].

The resonant mass is typically made of an alloy of aluminum and weighs several tons, but some have been made of niobium or single-crystal silicon or sapphire. To reduce thermal noise, the resonant mass is usually cooled to liquid-helium temperatures or below.

The resonant-mass antenna is instrumented with an electromagnetic transducer and electronics, which monitor the complex amplitude of one or more of the mass's normal modes. When a gravitational wave passes through the mass, its frequency components near each normal-mode frequency f_0 drive that mode, changing its complex amplitude; and the time evolution of the changes is measured within the bandwidth Δf by the transducer and electronics. In the past, resonant-mass antennas were narrow-band devices ($\Delta f/f_0 \ll 1$), but in the last few years, the efforts of researchers managed to increase the bandwidth [6] [7].

We will now have a closer look to bars and spheres.

Cylindrical Antennas

Bars have been the first gravitational waves antennas to be operated, and one of the reasons for this choice is the simplicity of the model, since (as will be clear below) a cylinder behaves as an harmonic oscillator. Since Weber time, the conceptual scheme of the detector has not been modified, but, thanks to technological progress, the sensitivity of these detectors has improved by a factor of one thousand.

Let us consider a cylinder of mass M and length L , with its axis par-

allel to the \mathbf{z} axis of our reference frame. We cut the bar into infinitesimal cylindrical slices of thickness dz . If we define $\xi(z, t)$ the relative movement at time t of two free-falling slides symmetrically located with respect to the centre of mass, it is straightforward to see that the equation obeyed by this quantity is

$$\rho \ddot{\xi} - Y \frac{\partial^2 \xi}{\partial z^2} - D \frac{\partial}{\partial t} \frac{\partial^2 \xi}{\partial z^2} = \frac{\rho z}{2} \ddot{h} \quad (1.4)$$

where ρ is the density of the bar, Y and D are respectively its Young modulus and dissipation coefficient. The term $\frac{\rho z}{2} \ddot{h}$ is the gravitational force. Using the Fourier transform $\chi(\omega, z)$ of $\xi(t, z)$ and imposing the right boundary conditions, the solution of equation (1.4) can be written as

$$\chi(\omega, z) = \frac{z}{2} H(\omega) - \frac{H(\omega)}{2} \frac{\sin \alpha z}{\alpha \cos \frac{\alpha L}{2}} \quad (1.5)$$

where $\alpha = \sqrt{\frac{\omega^2 \rho}{Y}} \sqrt{\left(1 - \frac{i}{Q}\right)}$ and $Q = \frac{Y}{\omega D}$ is mechanical quality factor of the bar. So it is easy to see that the transfer function of the bar is [4]

$$T_b = \frac{1}{2} \left(z - \frac{\sin \alpha z}{\alpha \cos \frac{\alpha L}{2}} \right) \quad (1.6)$$

that has resonances for $\omega_k = (2k + 1) \omega_0$ with $k \in N$, $\omega_0 = \frac{\pi v}{L}$ and $v = \sqrt{\frac{Y}{\rho}}$ is the speed of sound of the bar. We notice that only odd harmonics are excited by gravitational radiation due to its quadrupolar nature. Since the distance between two consecutive harmonics is usually

very large, we can compute equation (1.6) in the limit $\omega \rightarrow \omega_0$ and $Q \gg 1$, and neglecting the z term, one finds

$$T_b \cong \frac{L\omega_0 \sin \alpha z}{\pi^2 \left(\omega - \omega_0 - \frac{i\omega_0}{2Q} \right)} \quad (1.7)$$

By calculating, in the same approximations, the transfer function of an harmonic oscillator of equation $\ddot{\xi} + 2\beta_1\dot{\xi} + \omega_0^2\xi = \frac{l}{2}\ddot{h}$ we find

$$T_0 \cong \frac{l}{4} \left(\frac{\omega_0}{\omega - \omega_0 - \frac{i\omega_0}{2Q}} \right) \quad (1.8)$$

Looking carefully to equations (1.7) and (1.8), it is evident [18] the analogy between a cylindrical bar and a simple harmonic oscillator. Actually the two transfer functions equal when we put $\frac{l}{4} = \frac{L}{\pi^2} \sin \alpha z$. So we can write the solution of the motion equation of a cylindrical bar near the first resonance frequency as

$$\xi(z, t) = -\frac{2L}{\pi^2} H(\omega_1) \omega_0 e^{-\beta_1 t} \sin(\omega_0 t) \sin\left(\frac{\omega_0 z}{v}\right) \quad (1.9)$$

This oscillation has a maximum at the ends of the bar and is zero at its center (see figure (1.5))

Another important parameter in the study of the interaction between gravitational waves and a cylindrical bar is the cross section. In the case of an h_+ wave coming from any direction, the cross section is found to

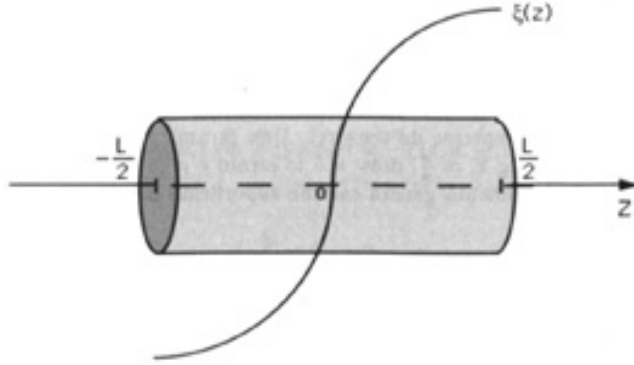


Figure 1.5: The amplitude of the oscillation of a bar as a function of z .

be [4]

$$\Sigma_{\theta\varphi} = \frac{16Gv^2}{\pi c^3} M \cos^4 \theta \sin^2 2\varphi \quad (1.10)$$

And when it is averaged over all possible directions of the impinging wave

$$\Sigma = \frac{32}{15\pi} \frac{GM}{cn^2} \left(\frac{v}{c}\right)^2 \quad (1.11)$$

Spherical Antennas

The next generation of resonant-mass gravitational wave detectors will have spherical shape. At present, two of these detectors are being built, Mario Shenberg [10] (Sao Paulo, Brasil) and MiniGRAIL [9] (Leiden, The Netherlands). Both are spheres made of an alloy of copper and aluminum with a diameter of 65 cm and a mass of 1150 kg and a resonant frequency of 3160 Hz. The goal sensitivity of these detectors is $h \simeq 10^{-20}$.

Spheres have several advantages with respect to bars. First of all,

a spherical detector is omni-directional, it is equally sensitive to a wave from any direction and it can also measure the polarization state of the wave. A single sphere is able to determine the source direction [19]. Besides, as will be shown below, the energy cross-section of a sphere is about 70 times larger than a typical bar at the same resonant frequency. Furthermore, the spherical geometry can, in principle, help in discriminating between different metric theories of gravity [20].

According to the classical theory of elasticity, it is possible to see [21] that the eigenfunctions of the quadrupolar modes can be written as a combination of spherical harmonics

$$\Psi_{lm} = [\alpha_l(r)\hat{\mathbf{r}} + \beta_l(r)R\nabla]Y_{lm}(\theta, \phi) \quad (1.12)$$

where l is odd and $\alpha_l(r)$ and $\beta_l(r)$ are the radial eigenfunctions and determine the motion in the radial and tangential directions respectively. We can describe the interaction of a gravitational wave with a body as a “tidal” force density

$$f_i^{GW}(\mathbf{x}, t) = \frac{1}{2}\rho \sum_j \frac{\partial^2 h_{ij}(t)}{\partial t^2} x_j \quad (1.13)$$

The gravitational effective force F_m^s for the mode m of the sphere is given by

$$F_m^s \equiv \int_{V_0} \Psi_m \cdot \mathbf{f}^{GW} d^3\mathbf{x} \quad (1.14)$$

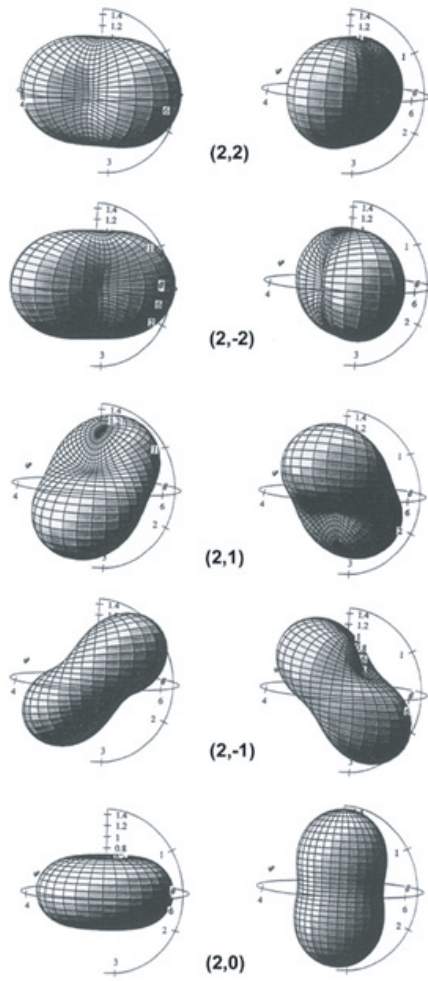


Figure 1.6: The deformation of the 5 quadrupolar modes of a sphere. For each mode we show two deformations differing by half a period.

So, using equations (1.12) and (1.13) we find

$$F_m^s(t) = \frac{1}{2} \ddot{h}_m(t) m_s \chi R \quad (1.15)$$

Thus we can think the effective force F_m^s as the product of the mass of the sphere m_s , an effective length χR and the gravitational acceleration $\frac{1}{2} \ddot{h}_m$, where we use h_m to denote the 5 amplitudes of the gravitational wave. So from equation (1.15) we can infer that there is an univocal correspondence between the 5 quadrupolar modes of a sphere and the 5 amplitudes of a gravitational wave. So, thanks to a spherical detector, it would be possible to measure all the components of the tensor h_{ij} and thus to discriminate between different metric theories of gravity.

The total cross section of a sphere for each quadrupolar mode is given by [22]

$$\sigma_n = F_n \frac{G}{c^3} M_s v_s^2 \quad (1.16)$$

where n is the order of the quadrupole mode, M_s is the sphere mass, v_s the sound velocity and F_n is a dimensionless coefficient characteristic of each quadrupole mode. It is interesting to note that the cross section of the second-order quadrupolar mode is only a factor 2.61 lower than that of the first-order quadrupole mode. This means this detector can potentially be used at two frequencies.

It has been known for some time that a sphere has a gravitational cross section 18 times larger than that of an equivalent bar at the same

frequency [19] for a single component of the gravitational tensor. This statement, however, ignores the fact that a sphere can detect all 5 independent components of the gravitational strain tensor, compared to only one for the bar. For a bar detector, it is well known that averaging over source direction and polarization [15] leads to a loss of energy resolution, compared to the optimum, by a factor $15/4 = 3.7$. Thus the net result is that the angle-averaged energy resolution of a sphere is $3.7 \times 18 = 67$ times better than the equivalent bar detector (or about 8 times in h).

Chapter 2

Resonant Mass Detectors

2.1 On the sensitivity of a bar detector

Any vibrational mode of a resonant body that has a mass quadrupole moment, such as the fundamental longitudinal mode of a cylindrical antenna, can be excited by a gravitational wave (GW in the following) with nonzero energy spectral density at the mode eigenfrequency.

The size of a resonant antenna is determined by the frequency and the velocity of sound v_s in the material used. Since v_s is always orders of magnitude less than the speed of propagation of gravitational radiation, resonant-mass antennas are always much smaller than the wavelength of the radiation. Typical antennas are thin cylindrical bars made of aluminum with a fundamental longitudinal resonance in the frequency band around 1 kHz.

Because of the forces responsible for the antenna's elasticity, the GW performs work and, in the case of a thin cylindrical bar, deposits energy only in the odd-order longitudinal modes. Because of the quadrupole nature of the radiation, the even-order modes are not excited.

The mechanical oscillation induced in the antenna by interaction with the GW is transformed into an electrical signal by a motion or strain transducer and then amplified by an electrical amplifier.

Equations governing the motion of a bare cylindrical bar have already been given in Section 1.2.2.

2.1.1 The motion sensor

After a signal has been picked up by the antenna, it must be amplified and recorded for analysis. The only viable way to achieve this is to transform the signal into electromagnetic energy, and then use state-of-the-art techniques for electromagnetic amplification and read-out.

The electromechanical transducer can be represented with the components of the Z_{ij} matrix which connects the input variables (force $f(t)$ acting on the transducer and velocity $\dot{x}(t)$ of the transducer mechanical parts) with the output variables (voltage $v(t)$ and current $i(t)$):

$$f(t) = Z_{11}\dot{x}(t) + Z_{12}i(t) \tag{2.1}$$

$$v(t) = Z_{21}\dot{x}(t) + Z_{22}i(t) \tag{2.2}$$

In important cases the Z_{ij} components satisfy the relationships $Z_{11}Z_{22} = Z_{12}Z_{21}$ and $Z_{12} = Z_{21}$.

An important parameter is the ratio β of the electrical energy in the transducer to the total energy in the resonant body:

$$\beta = \frac{1}{m\omega} \frac{|Z_{21}|^2}{Z_{22}} \quad (2.3)$$

The principle of all transducers is to store electromagnetic energy in a very small volume, usually a narrow gap, one of the walls of which is part of the antenna. The motions of this wall, arising from vibrations in the antenna, induce a modulation of this energy which is detected and amplified as an electrical signal. Transducers of the sensitivity required to detect the extremely small signals of gravitational radiation are not available commercially. Development of transducers and components of the read-out system are therefore an important part of the R&D efforts of all gravitational wave experiments.

Strain transducers are classified as belonging to the following three categories: capacitive (electrostatic), inductive (magnetostatic), optical (electromagnetic).

Piezo-electric, magnetostrictive and μ -wave cavities are respective examples of such transducers. We can also distinguish between passive and active transducers. Passive transducers are linear transducers in which the source of energy in the gap is a permanent field, either electric or magnetic or both. These transducers preserve a linear phase and am-

plitude relation between input and output. Because of their relatively simple construction they are widely used.

In active transducer the gap is fed with an oscillating bias field at high frequency ω_p . The mechanical vibration of frequency ω_0 modulates the phase of this oscillating field and produces side-bands which contain the information of the mechanical signal. Good performance of this type of transducer is expected because of the gain ω_p/ω_0 resulting from the conversion of the pump frequency ω_p into the antenna frequency ω_0 .

An important breakthrough in increasing the sensitivity of resonant-mass detectors was achieved when resonant transducers were introduced [25] (which can be active or passive).

In a resonant mass transducer an oscillator with a small effective mass m_t is coupled in resonance with the antenna, which has a large effective mass m . The maximum amplitude of the motion of the small oscillator will then be increased by a factor $\sqrt{m/m_t}$ relative to the amplitude of the antenna. In the expression of β the antenna mass is thus replaced by the transducer mass.

Several groups have analyzed resonant transducers and have developed their own designs [25, 26, 27, 28].

The transducer is connected to an electrical amplifier whose noise can be characterized by two parameters. The two parameters are, usually, the power spectra of the voltage and current noise, V_n^2 and I_n^2 , or their

following combinations:

$$T_n = \frac{\sqrt{V_n^2 I_n^2}}{K} \quad (2.4)$$

$$R_n = \sqrt{\frac{V_n^2}{I_n^2}} \quad (2.5)$$

T_n is called the amplifier noise temperature and R_n the amplifier noise resistance. Another parameter, useful to express the matching between transducer and amplifier, is

$$\lambda = \frac{R_n}{|Z_{22}|} \quad (2.6)$$

A large fraction of the technological complexity of resonant mass detectors results from the optimization of the quantities β , T_n and R_n .

2.1.2 Noise

Two classes of noise source have to be considered in the sensitivity analysis of a GW antenna:

- the intrinsic noise sources such as the thermal and electronic ones, which have Gaussian statistics and can be accurately modeled, and
- the external noise sources such as seismic noise and disturbances from cosmic rays, which are more difficult to characterize because they are non-Gaussian and often also non-stationary.

The tail of the Gaussian distribution and the effects of the external noise can be efficiently eliminated by coincidence measurements with several detectors located far away from each other.

The thermal, or Brownian, noise is due to chaotic motion of the detector atoms in the thermal bath at the temperature T . The power spectrum of the stochastic force acting on the oscillator is

$$S_F(\omega) = 4\beta_1 mkT \quad (2.7)$$

The electronic noise has two terms: one is the back action stochastic force exerted by the current noise generator. This acts on the oscillator like the Brownian force, with a power spectrum

$$S_f = |Z_{12}|^2 I_n^2 = m\beta\omega_0 |Z_{22}| I_n^2 \quad (2.8)$$

The effect of the back action noise can be seen as an increment to the oscillator temperature T . The sum of Brownian noise of the oscillator at temperature T and back action noise can be attributed to the Brownian noise of an oscillator at temperature $T_e > T$ where [4]

$$T_e = T \left(1 + \frac{\beta Q T_n}{2\lambda T} \right) \quad (2.9)$$

The other term is an additive noise due to amplifier, its power spectrum is

$$S_0 = V_n^2 + I_n^2 |Z_{22}|^2 = kT_n |Z_{22}| (\lambda + 1/\lambda) \quad (2.10)$$

If the Z_{22} impedance is a smooth function of the frequency, the power spectrum S_0 can be considered white in the antenna bandwidth.

Another convenient dimensionless parameter is

$$\Gamma = \frac{T_n(\lambda + 1/\lambda)}{2\beta QT_e} \quad (2.11)$$

that gives the ratio of the wide band noise in the resonance band width to the narrow band noise (in practice $\Gamma \ll 1$).

The sum at the output of the contributions given by the Brownian noise (at temperature T_e) and by the wide band electronic noise gives the total detector noise. This can be referred to the input of the detector (as if it were a GW spectral density) and is usually indicated as $S_h(f)$. This function as a simple analytical expression showing an anti-resonance at f_0 [29]. It can be written as:

$$S_h(f) = \frac{4T_e(2\pi f_0)}{\frac{1}{2}ml^2Q(2\pi f)^4} \left\{ 1 + \Gamma \left[Q^2 \left(1 - \frac{f^2}{f_0^2} \right)^2 + \frac{f^2}{f_0^2} \right] \right\} \quad (2.12)$$

$S_h(f)$ represents the input GW spectrum that would produce a signal equal to the noise spectrum actually observed at the output of the antenna instrumentation. This function is independent of any assumption about the signal waveform. The half height width of this function gives the bandwidth of a resonant detector:

$$\Delta f = \frac{f_0}{Q\sqrt{\Gamma}} \quad (2.13)$$

This is much larger than the pure resonance linewidth f_0/Q . It is interesting to note that in the limit $\Gamma \rightarrow 0$, expression (2.12) can be obtained by simply equalizing the power spectrum of the stochastic force $4kT_e m \beta_1$ to the power spectrum of the GW induced force $(m\omega^2 l/2)^2 S_h$. In this limit the bandwidth becomes infinite. A natural way to express $S_h(f_0)$ is by means of the total integrated cross section:

$$S_h(f_0) = \frac{G}{c^3} \frac{4kT_e}{\sigma_{tot} Q f_0} \quad (2.14)$$

Equation (2.12), or (2.13) and (2.14), characterizes completely the sensitivity of a resonant-mass detector.

2.1.3 SNR

The problem of extracting a signal $h(t)$ from a noise with given spectrum $S_h(f)$ is deeply treated in the information theory.

The optimum performance of a detector is obtained by filtering the output with a filter matched to the signal. The energy signal-to-noise ratio (SNR) of the output of the filter is given by the well known formula [30]

$$SNR = \int_{-\infty}^{+\infty} \frac{|H(f)|^2}{S_h(f)} d\omega \quad (2.15)$$

where $H(f)$ is the Fourier transform of $h(t)$. Although the integration range is infinite in theory, in practice it will be reduced to the Nyquist band for any specified set of sampled data. For a sampling interval Δt ,

the Nyquist band is $(-1/2\Delta t, 1/2\Delta t)$.

Let us consider the SNR for various GW signal.

- **Burst**

We model the burst signal as a featureless waveform, rising quickly to an amplitude h_0 and lasting for a time τ_g much shorter than the detector integration time $\Delta t = \Delta f^{-1}$. Its Fourier transform will be considered constant within the detector bandwidth Δf : $H(f) \simeq H(f_0) = H_0 \simeq \frac{1}{2}h_0\tau_g$. From the eq (2.15) we get:

$$SNR = \frac{\frac{1}{2}m(2\pi f_0)^4 l^2 H_0^2}{4kT_e\sqrt{\Gamma}} \quad (2.16)$$

The numerator is the energy that the burst would have deposited in the detector mode if it had been initially unexcited. The denominator characterizes the overall noise in the detector and is usually expressed as kT_{eff} . The minimum detectable value of H_0 (SNR = 1) can then be written as

$$H_0^{min} = \left[\frac{kT_{eff}}{\frac{1}{2}ml^2(2\pi f_0)^4} \right]^{1/2} \quad (2.17)$$

and the minimum GW amplitude h_0^{min} is equal to $2\tau_g^{-1}H_0^{min}$. As for T_{eff} , it can be written in a convenient way as

$$T_{eff} = 4kT_e\sqrt{\Gamma} \simeq 2\sqrt{2}T_n \left(1 + \frac{2T}{\beta QT_n} \right)^{1/2} \quad (2.18)$$

where the approximate equality holds if we put $\lambda \simeq 1$. The strategy to optimize burst detection is to have T_n as small as possible while satisfying the condition $\beta QT_n \gg T$ (brownian noise negligible respect to the amplifier noise). This condition makes desirable a strong coupling of the transducer to the antenna, widening the detection bandwidth. In fact, the bandwidth Δf , taking into account equations (2.9) and (2.11), can be rewritten as ($\lambda = 1$)

$$\Delta f = 2^{-1/2} f_0 \beta \left(1 + \frac{2T}{\beta QT_n} \right)^{1/2} \quad (2.19)$$

If β approaches unity, the bandwidth may become as large as f_0 . The limit (obtainable with $\lambda \gg 1$) $T_{eff} = 2T_n$ expresses the so called amplifier limit for burst detection. This limit cannot be surpassed, except using back action evading techniques. As discussed by Giffard [24] in the context of GW detectors, any linear amplifier is limited by the uncertainty principle to a noise temperature greater than $\hbar\omega_0/k$, leading to a fundamental sensitivity limit on the burst noise temperature of a resonant-mass GW detector given by $T_{eff} > \hbar\omega_0/k$, which is equal to 50 nK at 1 kHz.

From eq (2.15) we can derive the relation between the sensitivities expressed in term of spectral amplitude $\sqrt{S_h(f_0)}$, which has units

Hz^{-1/2}, and the dimensionless burst amplitude h_0^{min} [29]:

$$SNR = \frac{2\pi\Delta f H_0^2}{S_h(f_0)} \quad (2.20)$$

for SNR = 1, and using the equation (unilateral) $H_0^{min} = h_0^{min}\tau_g$, we find

$$h_0^{min} = \tau_g^{-1} \left[\frac{S_h(f_0)}{2\pi\Delta f} \right]^{1/2} \quad (2.21)$$

- **Monochromatic**

We consider a sinusoidal wave of amplitude h_0 and frequency f_g constant for the entire observation time t_m . The Fourier transform amplitude at f_0 is $\frac{1}{2}h_0t_m$ with a bandwidth given by t_m^{-1} . The SNR can be written as

$$SNR = \frac{\frac{1}{4}m(2\pi f_g)^4 l^2 h_0^2 t_m Q}{4kT_e(2\pi f_0)} \{1 + \Gamma [Q^2 (1 - f_g^2/f_0^2) + f_g^2/f_0^2]\} \quad (2.22)$$

The SNR bandwidth Δf is given by eq. (2.13). For SNR = 1 we obtain the minimum detectable value of h_0 , which at $f_g = f_0$ is

$$h_0^{min} = \left[\frac{4kT_e}{\frac{1}{4}ml^2(2\pi f_g)^3 Q t_m} \right]^{1/2} \quad (2.23)$$

The detection of continuous signals places different requirements respect to the burst detection case. The strategy here is to reduce

T_e to the sole contribution of the Brownian noise, making negligible the electronic noise, i.e. $T \gg \beta Q T_n$, and lower T as much as possible. In this case the requirement on the antenna-transducer coupling is less severe than in the burst detection case. Actually a weak coupling helps the thermal noise to be dominant. Following this strategy one gets a smaller bandwidth. This is not surprising, as the usual optimization for monochromatic signal detection prescribes to maximize the SNR of the instrument over a narrow bandwidth centered on the signal frequency f_s (of course this requires knowledge of f_s). For instance the nearby pulsar [31] PSR J0437-4715, at a distance of 150 pc, should emit at 347 Hz a GW amplitude (optimistically) of $2 \cdot 10^{-26}$. This would give $\text{SNR} = 1$ on a resonant-mass bar of $M = 10$ ton, $Q = 10^7$, $T_e \simeq T = 20$ mK, after integrating the signal for 1 year.

- **Chirp**

The gravitational waveform of increasing amplitude and frequency emitted by a compact binary system (consisting of either neutron stars or black holes) in the inspiral phase, when the two stars get closer and closer as a result of GW emission caused by their orbital motion, is called chirp [32, 33]. Binary systems have received a lot of attention as GW sources because of the existence of PSR 1913 + 16 and of the clean analytic behaviour of the emitted GW. If the masses of the two compact objects are small enough (a few

solar masses) the chirp signal sweeps up to the kHz region of frequency and then can excite resonant-mass detectors. From the resonant-mass detector viewpoint, the chirp signal can be treated as a transient GW, depositing energy in a time-scale short respect to the detector damping time τ [34]. We can then use eq. (2.15) to evaluate the SNR, where the Fourier transform $H(f_0) \equiv H_0$ at the resonant frequency f_0 can be explicitly written as

$$H_0 = \left\{ \left[\int h(t) \cos(2\pi f_0 t) dt \right]^2 + \left[\int h(t) \sin(2\pi f_0 t) dt \right]^2 \right\}^{1/2} \quad (2.24)$$

Substituting in (2.24) the well known chirp waveforms for optimally oriented orbit of zero eccentricity [15], the SNR for chirp detection is:

$$SNR = \frac{2^{1/3} 5}{48} G^{2/3} \frac{\sigma_{tot}}{kT_{eff}} \frac{1}{r^2} M_c^{5/3} (2\pi f_0)^{-1/3} \quad (2.25)$$

M_c is the chirp mass defined as $M_c = (m_1 m_2)^{3/5} (m_1 + m_2)^{-1/5}$, m_1 and m_2 are the masses of the two compact objects and r is the distance to the source. For example, a system of two neutron stars or black holes having $m_1 = m_2 = 1.4 M_\odot$ at 10 Mpc distance will give $SNR = 1$ in an aluminum cylindrical bar of mass $M = 2.3$ ton resonating at $f_0 = 915$ Hz and having $kT_{eff} = 2\pi\hbar f_0$.

- **Stochastic background**

In this case $h(t)$ is a random function and we assume that its power

spectrum, indicated by $S_{gw}(f)$, is flat and its energy density per unit logarithmic frequency is a fraction $\Omega_{gw}(f)$ of the closure density ρ_c of the universe:

$$\frac{df_{gw}}{d \ln f} = \Omega_{gw} \rho_c \quad (2.26)$$

$S_{gw}(f)$ is given by

$$S_{gw}(f) = \frac{2G}{\pi} f^{-3} \Omega_{gw}(f) \rho_c \quad (2.27)$$

The measured $S_h(f)$ of a single resonant detector gives automatically an upper limit to $S_{gw}(f)$ (and hence to $\Omega_{gw}(f)$). Two different detectors with overlapping bandwidth Δf will respond to the background in a correlated way. The SNR of a GW background in a cross-correlation experiment between two detectors located near one another and having power spectral density of noise $S_h^1(f)$ and $S_h^2(f)$ is [35]

$$SNR = \left(\frac{S_{gw}^2}{S_h^1 S_h^2} \Delta f t_m \right)^{1/4} \quad (2.28)$$

where t_m is the total measuring time. Detectors that are separated by some distance are not as well correlated, because GW coming from within a certain cone about the line joining the detectors will reach one detector well before the other. The fall-off in the correlation with separation is a function of the ratio of the wavelength to the separation, and it has been studied for pairs of bars and pairs of

interferometers [36, 37]. Supposing two identical detectors are co-located and aligned for optimum correlation, the background will reach a $\text{SNR} = 1$ if Ω_{gw} is

$$\Omega_{gw} \simeq 2 \cdot 10^{-5} \left(\frac{f_0}{1 \text{ kHz}} \right)^3 \left(\frac{\sqrt{S_h^1(f_0) S_h^2(f_0)}}{10^{-46} \text{ Hz}} \right) \left(\frac{10 \text{ Hz}}{\Delta f} \right)^{1/2} \left(\frac{10^7 \text{ s}}{t_m} \right)^{1/2} \quad (2.29)$$

where the Hubble constant is assumed to be $100 \text{ km s}^{-1} \text{ Mpc}^{-1}$. Equations (2.28) and (2.29) hold for whichever cross-correlation experiment between two GW detectors adjacent and aligned for optimum correlation. An interesting consequence is that it may be worthwhile in the near future to move an advanced resonant mass detector very near to a large interferometer to perform stochastic searches near 1 kHz [38].

2.2 A brief history of bar detectors

Joseph Weber [23], back in the ‘60s, was the pioneer of resonant-mass detectors. His antennas were bare aluminum cylinders, read by piezo-electric ceramics. His work stimulated other groups to start this kind of research. But people working on gravitational waves, soon realized that room temperature detectors would not be sensitive enough for gravitational waves detection.

Cryogenic resonant-mass detectors were conceived in the ‘70s with the aim of improving the sensitivity of the room temperature Weber

detectors by many orders of magnitude, by reducing the temperature of the resonant-mass to or below liquid helium temperature (4.2 K) and employing superconducting electronic devices in the readout system.

The first cryogenic detector was operated at the beginning of the ‘80s by the Fairbank group in Stanford [39], followed by the Rome group detector EXPLORER [40] placed at CERN and by the LSU group detector ALLEGRO [41]. Already in 1986 these three cryogenic detectors have put an upper limit on GW bursts bathing the Earth [42]. Only at the beginning of the ‘90s, however, the cryogenic detectors entered in the continuous operational mode and hence in the field of reliable instruments of physics. The Stanford detector, damaged by the 1989 earthquake, was shut down. Another detector, called NIOBE, started operating in Perth [43] in 1993. In table (2.1) we give a summary of the presently operating cryogenic detectors. The date of the data taking indicates the initial time of the detector continuous operation, although sometimes this moment has been preceded by tests with various periods of data taking alternated by the upgrading of the apparatus.

The sensitivities refer to a GW burst lasting 1 ms. All the detectors are cylindrical bars. We remark that $h = 6 \cdot 10^{-19}$ corresponds to a millisecond GW burst due to the total conversion of about $10^{-4}M_{\odot}$ in the Galactic center. The spectral amplitude sensitivity is of $\sqrt{S_h} \simeq 10^{-21} \text{ Hz}^{-1/2}$ with bandwidth of a few Hz.

Duty cycles of cryogenic bars, including interruptions for periods of

Table 2.1: Main features of the operating cryogenic detectors. T_{eff} expresses (in Kelvin) the minimum detectable energy innovation and determines the detector sensitivity to short (1 ms) bursts, indicated with h^{min} .

	ALLEGRO	AURIGA	EXPLORER	NAUTILUS
material	Al5056	Al5056	Al5056	Al5056
length (m)	3.0	2.9	3.0	3.0
M (kg)	2296	2230	2270	2260
f_- (Hz)	895	912	905	926
f_+ (Hz)	920	930	921	941
$Q \times 10^6$	2	3	1.5	0.5
T (K)	4.2	0.25	2.6	3.5
$S_h(f)^{1/2}$	$1 \cdot 10^{-21}$	$2 \cdot 10^{-22}$	$1 \cdot 10^{-21}$	$2 \cdot 10^{-22}$
Δf (Hz)	$\simeq 1$	$\simeq 1$	$\simeq 9$	$\simeq 6$
T_{eff} (mK)	10	2	2	2
h^{min}	$6 \cdot 10^{-19}$	$4 \cdot 10^{-19}$	$4 \cdot 10^{-19}$	$4 \cdot 10^{-19}$
latitude	30°27'00"N	44°21'12"N	46°27'00"N	41°49'26"N
longitude	268°50'00"	11°56'54"	6°12'00"	12°40'21"

maintenance, are better than 70%. We can confidently say that today the strongest sources in our Galaxy and in the local group will not pass unnoticed when at least two resonant-mass detectors are in operation.

This fact is extremely important as the search for GW is based on the technique of coincidences among two or more detectors. At present the cryogenic bars are aligned parallel to each other, so the same GW burst would produce in the detectors signal of the same amplitude.

Up to now the analysis of the data has been focused in searching for short GW burst [17, 56]. The data of each detector are filtered with matched filters for δ -like bursts. A list of energy innovations above a given (a priori) threshold and the corresponding occurrence times is then

produced for each detector. The number n_c of coincidences at zero delay in a given (a priori) time window Δt is compared with the number of accidental coincidences $\langle n \rangle$. This number can be calculated for the stationary cases with the formula

$$\langle n \rangle = \frac{N_1 N_2 \Delta t}{t_m} \quad (2.30)$$

where N_1 and N_2 are, respectively, the number of events for each of the two detectors in the period t_m of data taking. The probability to have n_c coincidences while expecting $\langle n \rangle$ can, of course, be estimated with the Poisson statistics.

A more general and model independent procedure is to determine experimentally this probability by looking for the coincidences $n_c(\delta t)$ obtained after shifting the time of occurrence of one detector by δt , and repeating this for N different values of δt , obtaining N numbers $n_c(\delta t)$. The accidental background is calculated from the average number of the n_{shift} shifted coincidences obtained from the N time shifts

$$\langle n \rangle = \frac{\sum_{j=1}^N n_{shift}(j)}{N} \quad (2.31)$$

This experimental procedure for evaluation of the background has the benefit of handling the problems arising when the distribution of the events is not stationary. No significant coincidences excess has been reported until now, except that in [56].

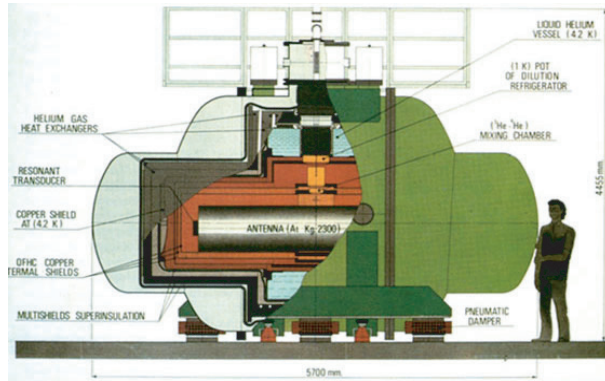


Figure 2.1: The layout of the NAUTILUS detector.

Among the remarkable performances of this generation of detectors it is worth mentioning the upper limits provided to the existence of exotic particles [44] (which passage through the bar should excite the vibrational mode) and the absolute calibration of the EXPLORER detector with the gravitational near field generated by a small mechanical rotor [45].

2.3 The ROG detectors

The ROG group operates two detectors: EXPLORER (at CERN) and NAUTILUS (at INFN Frascati National Laboratories). Both are cylindrical bars made of aluminum 5056, with a mass of 2350 kg, length of 3 m and diameter of 0.6 m. A layout of NAUTILUS is shown in figure (2.1). Inside to the external vacuum chamber, the cryostat contains two helium gas cooled shields, the liquid helium (LHe) reservoir (2000 liters of capacity), three OFHC copper massive shields and, through the top

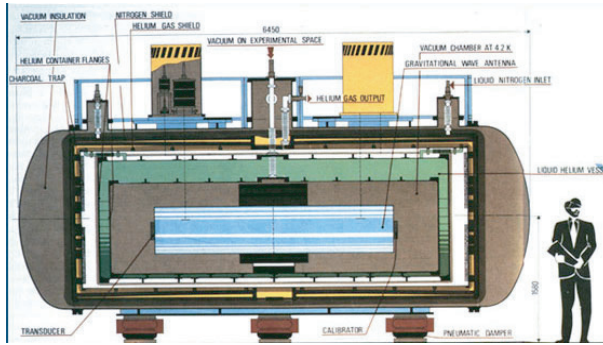


Figure 2.2: The layout of the EXPLORER detector.

central access, a special ^3He - ^4He dilution refrigerator [46, 47]. The shields are suspended to each other by means of titanium rods and constitute a cascade of low pass mechanical filters. The bar is suspended to the first shield by a U-shaped copper rod wrapped around the bar central section. The overall mechanical vibration isolation at the bar resonant frequency ($f_b = 915$ Hz) is of the order of -250 dB. The thermal path from the mixing chamber of the refrigerator to the bar is constituted by soft multiwire copper braids, connected to the ends of the copper suspension rod [48]. This detector has been the first massive body cooled at these very low temperatures.

The layout of EXPLORER (see figure (2.2)) is much similar to that of NAUTILUS, except that EXPLORER is not equipped with a dilution refrigerator. So the bar is cooled through thermal contact with the helium bath, which is kept at 2.6 K, below the superfluid transition.

The vibrations of the bars are converted into electrical signals by a

resonant capacitive transducer [49]. The signals are applied to the input coil of a dc SQUID amplifier by means of a superconducting transformer, which provides the required impedance matching. The capacitive transducer bolted to one end of the antenna consists of a vibrating disk with an effective mass $m_t = 0.750$ kg and of a fixed plate with a gap $d \simeq 10$ μm and a total capacitance $C_t \simeq 10$ nF. The transducer and the bar form a system of two coupled oscillators. The frequencies (f_- and f_+) of the resulting normal modes are spaced of about $f_b\sqrt{\mu}$, where μ is the ratio between the effective masses of the transducer disk and the bar.

The output signal from the SQUID instrumentation is sent to the data acquisition system, which is connected to the network and can be remotely operated. This machine performs the acquisition and the permanent recording of the data in a form suitable for further off-line analysis and various functions of on-line analysis for diagnostic purposes. The experimental apparatus includes a vibration sensor (accelerometer) located on the cryostat. This sensor monitors the environment of the laboratory. Its output signal may be used as a veto. Another signal, which is used as a veto, is the output of the antenna seen through the SQUID instrumentation and bandpass filtered between 20 and 70 Hz.

The detectors have also been equipped with a cosmic-ray veto system. For NAUTILUS the system consists of layers of streamer tubes [50] placed above and below the antenna cryostat. While EXPLORER has been equipped with plastic scintillators. The need for a cosmic rays detector

is due to the fact that extensive air showers or energetic single particles (muons or hadrons) interacting in the antenna may produce signals with rates which increase with the increasing sensitivity of the antenna to GW [51, 52, 53, 54]. For instance with a NAUTILUS sensitivity of $T_{eff} \sim 1$ mK, about 2 cosmic ray events per day are expected. This rate increases to about $5 \cdot 10^3$ if the quantum limit is reached.

Chapter 3

The read-out of NAUTILUS

The ultra-cryogenic GW detector NAUTILUS started its second science run in June 1998, after a partial overhaul of its mechanical suspensions and thermal contacts. We summarize here the results obtained during that run and the goals of the third science run, started in June 2003.

The results obtained from June 1998 to March 2002 show a considerable improvement in the rejection of non-stationary noise and in the sensitivity of the apparatus, with respect to the first science run 1995-1997 [55]. We show in figure (3.1) the strain sensitivity of the detector, expressed in units of $\text{Hz}^{-1/2}$. The sensitivity at the two resonances is about $4 \cdot 10^{-22}/\sqrt{\text{Hz}}$. The spectral amplitude is better than $3 \cdot 10^{-20}/\sqrt{\text{Hz}}$ over a band of about 25 Hz. The central peak at 914.6 Hz is a calibration signal fed into the d.c. SQUID to monitor the gain of the electronics. We also show in figure (3.2) the detector noise temperature over a sample

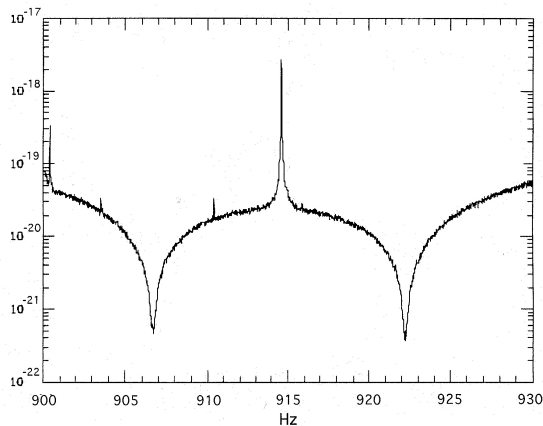


Figure 3.1: Experimental strain sensitivity of NAUTILUS in 1999 (input noise spectral amplitude in units of $\text{Hz}^{-1/2}$).

periods of two days. This sensitivity allows the detection, at $\text{SNR} = 1$, of an impulsive GW signal of duration 1 ms at amplitude $h \simeq 4 \cdot 10^{-19}$.

For the third science run we upgraded the NAUTILUS with a new bar, resonating at 935 Hz, and a new read-out system, similar to the one which is showing very good performances on EXPLORER [7]. The read-out consists of the new rosette transducer, a new high-Q superconducting transformer and a Quantum Design d.c. SQUID.

The goals of this run are to confirm the result of the coincidence analysis performed on the data of 2001 [56] and to get an unprecedented sensitivity for continuous signals at the frequency of 935 Hz.

The study of the coincidences between the GW detectors EXPLORER and NAUTILUS during 2001, showed an important result. With the 2001 data, an interesting coincidence excess is found when the detectors are

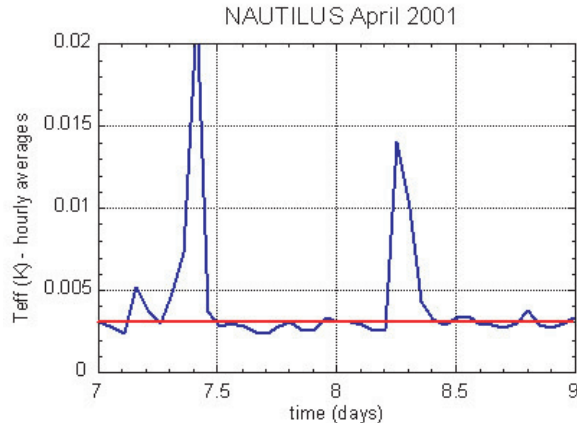


Figure 3.2: The detector noise temperature versus time, averaged over 1 hour, for a period of two days of 2001. The red line corresponds to a $T_{eff} \simeq 3$ mK. The peaks are due to a daily cryogenic operation.

favourably oriented with respect to the galactic disc (see figure (3.3)). The energy of the signals associated with the coincidences is, roughly speaking, about 100 mK. This corresponds, using the expression for the the classical cross-section (see equation (1.11)), to a conventional burst with amplitude $h \simeq 2 \cdot 10^{-18}$ and to the isotropic conversion into GW energy of $4 \cdot 10^{-3} M_{\odot}$, with sources located at a distance of 8 kpc. The observed rate is much larger than what the models available today predict for galactic sources. We note, however, that this rate of events is within the upper limit determined by IGEC for short GW bursts [57].

As can be seen from equation (2.20), to increase the SNR one must increase the strain sensitivity and bandwidth of the detector. This means

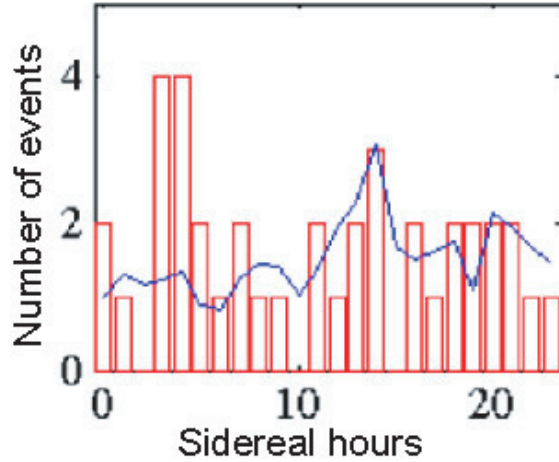


Figure 3.3: Result of the coincidence analysis. The graph shows the number of coincidences n_c indicated by the red bars and the average number \bar{n} of experimental accidentals versus sidereal time.

acting on the parameter Γ and the ratio $T/\beta Q$.

Middleditch *et al.* [58] reported evidence of a faint optical pulsar, remnant of the SN1987A in the Large Magellanic Cloud. The measurements indicate that the pulsar has a period of 2.14 ms, modulation period of about 1000 s and a spindown rate of $2 \div 3 \cdot 10^{-10} \text{ Hz s}^{-1}$. The spindown of a normal pulsar is believed to be caused by magnetic dipole radiation and relativistic pulsar winds. However, the low luminosity reported in the electromagnetic spectrum of this pulsar and the fact that the relation between spindown rate and modulation period can be explained at the same time by the existence of a non-axisymmetric component of the moment of inertia, support the idea that the spindown can be caused by radiating GW.

In this case, we can estimate the amplitude of the GW as [59]

$$h \simeq 4.7 \cdot 10^{-26} \left(\frac{I}{1.1 \cdot 10^{45} \text{ g cm}^2} \right) \left(\frac{\epsilon}{10^{-6}} \right) \left(\frac{f_g}{935 \text{ Hz}} \right)^2 \left(\frac{50 \text{ kpc}}{D} \right) \quad (3.1)$$

where I is the moment of inertia of the neutron star, ϵ its non-axisymmetric oblateness, D its distance from the Earth and f_g the frequency of the GW signal (twice the pulsar rotational frequency).

We now evaluate the sensitivity of the NAUTILUS required to observe such a signal. From equations (2.15) and (2.22), the SNR on the resonance can be written as

$$SNR = \frac{\frac{1}{2} h_0^2 t_m^2}{S_h(f_0)} \quad (3.2)$$

where we consider a sinusoidal wave of amplitude h_0 and frequency f_g , constant for the entire observation time t_m .

The value of h_0 from the signal of the pulsar in SN1987A, detectable with SNR=1, is $h_0^{min} = 4.6 \cdot 10^{-26}$ at 935 Hz. This value can be reached with a peak strain sensitivity of $6 \cdot 10^{-23} \text{ Hz}^{-1/2}$, integrating the signal for 1 month.

The detection of a continuous signal of known frequency places different requirements with respect to the strategy for burst detection. A large bandwidth is not required, but again the effort must be focused on achieving the lowest possible value of the factor T/Q .

As can be seen from picture (3.4), the read-out of a GW detector is

made of several parts, the most important are: the resonant transducer (developed at the University of Rome Tor Vergata), the superconducting transformer (developed at INFN Frascati National Laboratories) and the d.c. SQUID. But also the other components play an important role as

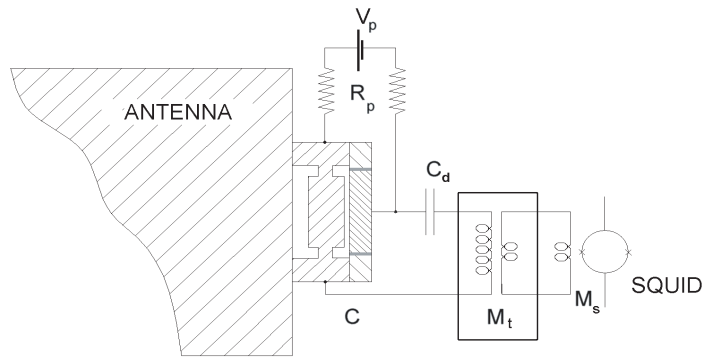


Figure 3.4: The read-out scheme of the EXPLORER and NAUTILUS detectors. In the box is the superconducting transformer and M_t is its mutual inductance, while C is the capacity of the resonant transducer. R_p are the polarization resistances and C_d is the decoupling capacitor needed to “charge” the transducer. M_s is the mutual inductance between the d.c. SQUID and its input coil.

we will see in the following. A part of the work of this thesis was focused on the problem of matching the electronic components of the read-out.

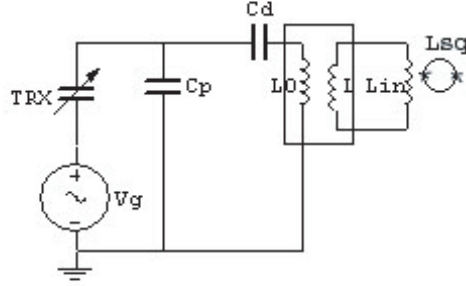


Figure 3.5: Scheme of the amplification electronic.

3.1 Influence of the electronic components on the sensitivity to bursts

As can be seen from equation (2.17), the quantity kT_{eff} characterizes the overall noise in the detector. The purpose of this section is to describe the role of the electronic components on the value of T_{eff} , which has to be as low as possible. From figure (3.5) we see that the capacitive transducer (C_t and its parasitic capacitance C_p) is coupled to the d.c. SQUID¹ via a superconducting high- Q transformer. The effect of the transduction can be represented by an equivalent voltage generator

$$v_g = E(y - x) \tag{3.3}$$

¹A detailed study of the d.c. SQUID will be done in the next Chapter.

where E is the electric field stored in the transducer and $y - x$ is the relative motion of the transducer with respect to the face of the antenna. We can neglect the losses of the superconducting transformer [60] because of the high Q and while the resonance frequency of the electrical mode is far from mechanical modes. Using the Thevenin Theorem, the voltage across the transducer is

$$v'_g = v_g \frac{C_t}{C_t + C_p} \quad (3.4)$$

By defining the following parameters:

- $M_1 = k_1 \sqrt{L_0 L}$ is the mutual inductance of the transformer and k_1 is its coupling coefficient;
- $M_2 = k_2 \sqrt{L_{in} L_{SQ}}$ and k_2 are the mutual inductance and the coupling coefficient between the d.c. SQUID and its input coil respectively;
- C_d is the decoupling capacitor, needed to charge the transducer;
- L_0 and L are the inductances of the primary and secondary coil of the transformer respectively;
- L_{in} is the inductance of the input coil of the SQUID and L_{SQ} that of the SQUID itself;
- $\gamma_s = \frac{L}{L + L_{in}}$.

It is possible to see that, neglecting the effect of the SQUID, the current flowing in the secondary coil is

$$i = v_g \left(\frac{C_t}{C_t + C_p} \right) \left(\frac{\sqrt{\frac{L_0}{L}}}{j\omega L_0 k_1 - \frac{1}{\gamma_s k_1} \left(\frac{1}{j\omega C} + j\omega L_0 \right)} \right) \quad (3.5)$$

where

$$C = \frac{C_d(C_p + C_t)}{C_p + C_t + C_d} \approx C_p + C_t \quad (3.6)$$

is the equivalent capacity as seen from L_0 , while the second equality is true only if $C_d \gg C_p + C_t$. By introducing the effective transformer ratio $N_e = \sqrt{\frac{L_0}{L}} k_1 \gamma_s$ we obtain

$$i = v_g \frac{C_t}{C_t + C_p} \frac{N_e}{Z_0(\omega)} \quad (3.7)$$

where the total impedance has been introduced

$$Z_0(\omega) = \frac{1}{j\omega C} + j\omega L_0(1 - \gamma_s k_1^2) = \frac{1}{j\omega C} \left(1 - \frac{\omega^2}{\omega_{el}^2}\right) \quad (3.8)$$

with the resonance frequency of the electrical mode

$$\omega_{el}^2 = \frac{1}{CL_0(1 - \gamma_s k_1^2)} \quad (3.9)$$

Now we can relate the magnetic flux in the SQUID, $\Phi = M_2 i$, with the mechanical signal

$$\Phi = M_2 i = \alpha_\phi (y - x) \quad (3.10)$$

and

$$\alpha_\phi = \frac{C_t}{C_t + C_p} \frac{N_e M_2}{Z_0(\omega)} = j\omega C_t \frac{N_e M_2}{\left(1 - \frac{\omega^2}{\omega_{el}^2}\right)} \quad (3.11)$$

We get the expected result² that, as long as $\omega_{el} > \omega_{\pm}$, (ω_{\pm} are the frequencies of the mechanical normal modes) α_{ϕ} does not depend on C_p .

Besides, it is clear that to maximize the signal fed to the SQUID it is necessary a transformer with a high coupling constant and a high effective transformer ratio.

In this case the parameter Γ , defined in equation (2.11), can be written as

$$\Gamma = \frac{\phi_n^2}{2\tau\Phi_{Br}^2} \quad (3.12)$$

and, accordingly, the signal on the SQUID due to the brownian noise is [60]

$$\Phi_{Br} = \alpha_{\phi} \sqrt{\frac{k_b T_e}{2m_y \omega_{\pm}^2}} \quad (3.13)$$

Inserting equations (3.11), (3.12) and (3.13) in equation (2.18), for T_{eff} one has

$$kT_{eff} = \frac{4\phi_n}{M_2 C_t E} \left[\frac{1}{N_e} \left(1 - \frac{\omega^2}{\omega_{el}^2} \right) \right] \sqrt{\frac{kT_e m_y}{\tau}} \quad (3.14)$$

Where ϕ_n is the intrinsic noise of the SQUID, m_y the mass of the transducer and τ is the common decay time of the modes.

From equation (3.14) it is clear that to minimize T_{eff} it is necessary to have a low noise (ϕ_n) and high coupling (M_2) d.c. SQUID, C_t as high as possible and a high τ . Since τ is related to the Q by the well known formula

$$Q = \pi\nu\tau \quad (3.15)$$

²The reasons why ω_{el} is kept higher than ω_{\pm} will be discussed in Section 3.2.

the last condition corresponds to a high Q . Both the bar and the transducer have Q s of the order of 10^6 and the overall Q of the detector is, roughly speaking, given by

$$Q_{tot}^{-1} \propto Q_{bar}^{-1} + Q_{trasd}^{-1} + Q_{el}^{-1} \quad (3.16)$$

In this sum the dominant term is the lowest, and, in the previous runs, Q_{el} has been of the order of 10^3 . So the necessity to increase Q_{el} by at least two order of magnitudes, is clear.

3.2 The superconducting transformer

The most important limiting factor of Q_{el} are the electrical losses of the superconducting transformer, arising from parasitic capacitance and dielectric losses of the coating of the wire. So the first step on the way to increase Q_{el} has been the realization of a truly high- Q superconducting transformer.

Other groups [61] have already investigated the issue of the realization of high- Q superconducting resonators. The work done in this section is very similar to that of [61], but it is also different in two fundamental aspects: the final goal and the measurement set-up. Here we intend to build a high- Q superconducting transformer, and we will see in the following that the current flowing in the secondary coil has a big influence on the quality factor of the resonator. Differences in the measurement

set-up will also be clear to the reader.

Since the superconducting transformer is needed to match the high output impedance of the transducer to the low input impedance of the SQUID, the values of the inductance of the primary coil (L_0) and that of the secondary coil (L) must fulfill the following conditions

$$\frac{1}{\omega C} = \omega L_0, \quad L = L_{in} \quad (3.17)$$

Since C is of the order of 10 nF and the working frequency of the detector is around 1 kHz, the perfect matching value of L_0 is [62] around 4 H, but in this case ω_{el} would be tuned to the mechanical modes. In this situation the three modes are highly coupled and can influence each other very deeply. Since the Q of the electrical mode varies with the working point of the d.c. SQUID, it is possible that also the Q s of the mechanical modes are influenced by the SQUID. To preserve the high intrinsic mechanical Q s, we decided to work with the electrical mode close but not tuned to the mechanical ones, so we agreed to build a superconducting transformer with $L_0 \simeq 2$ H. The value of L is determined by the SQUID used, but it is of the order of $1 \div 2 \mu\text{H}$.

The transformer must also be compact, as the box in which it is housed together with the SQUID, the decoupling capacitor and the polarization resistances, is quite small. Besides, the dimensions of the holder must be designed in such a way to take into account the fact that the spools of Nb wire available are 1 km long.



Figure 3.6: Picture of the transformer before insertion in the PVC box. It is possible to notice the weldings on the primary coil.

The inductance of the primary coil is a complex function of the following parameters: the diameter and the length of the holder; the number of layers and the number of turns on a single layer. So we wrote a code with Matlab[®]³ that uses formulas and tables of [63] to determine all these parameters. The holder (see figure (3.7)) is made of Teflon PTFE. We used Nb wire coated with FORMVAR[®] 80 μm thick and 1 km long. The number of turns per layer is 170, spaced by 20 μm , the number of layers is 55 and the total number of turns is 9317. To minimize the parasitic capacitance, we inserted a Teflon PTFE foil, 90 μm thick, to increase the distance between each layer.

Since the Nb wires are very thin and fragile, we welded them on two Nb foils, 100 μm thick, with a capacitive discharge welder. Then, on the

³See Appendix A for an example.

same foils and with the same technique, we welded a twisted pair of Nb wires, $125\ \mu\text{m}$ thick, inserted in two Teflon tubes. Furthermore, since Nb cannot be soft-soldered, we welded the ends of the pair on two Cu foils, $50\ \mu\text{m}$ thick, and then plated with SnPb. We performed an inductance measurement at room temperature⁴, getting $L_0 = 2.36\ \text{H}$, against the expected value of $2.35\ \text{H}$. Then we inserted the transformer into a PVC box. To minimize the effect of external magnetic fields, this box has been totally enclosed in two Pb shields⁵. Another effect of these shields is that they couple with the transformer lowering the value of the inductance of the primary coil. This effect becomes larger as the shields get closer to the transformer. Once the transformer has been cooled to liquid helium temperature ($4.2\ \text{K}$) we repeated the inductance measurement obtaining $L_0 = 2.09\ \text{H}$.

But the most important measurement is that of the Q . To perform this measurement we built an LC circuit and observed the decay of the resonant mode. Figure (3.8) shows the experimental setup. Two requirements must be fulfilled: the coupling between the pick-up coil (L_p) and L_0 must be very low (10^{-3} or less) in order not to perturb the decay; the capacitor must be a high- Q one⁶.

Since the capacitor has a capacitance of $C = 8.91\ \text{nF}$ at $4.2\ \text{K}$, we expected a resonance at $\nu = 1166\ \text{Hz}$. The measured frequency of the

⁴All the measurements are done with the HP4192A LCR Meter.

⁵The Pb becomes superconducting below $7.2\ \text{K}$.

⁶The high- Q Teflon capacitors have been bought from Eurofarad, 75540 Paris Cedex 11, France.

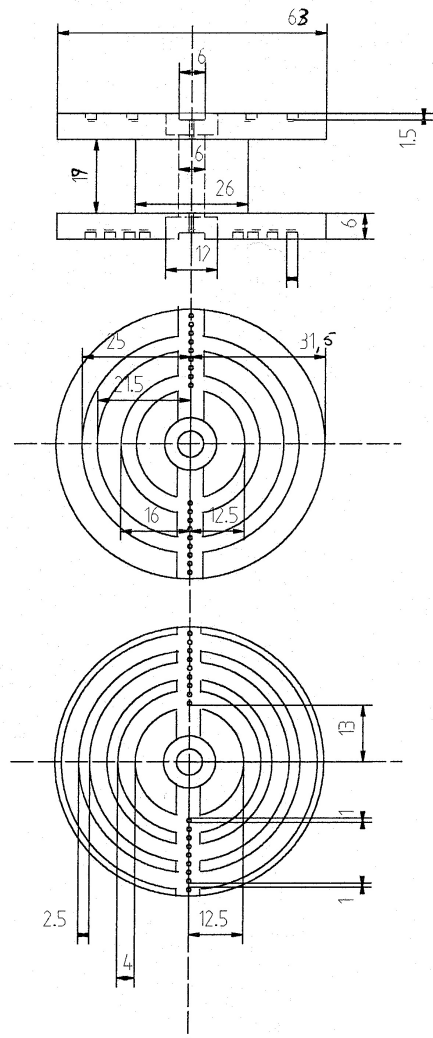


Figure 3.7: Design of the transformer holder, all measures are mm.

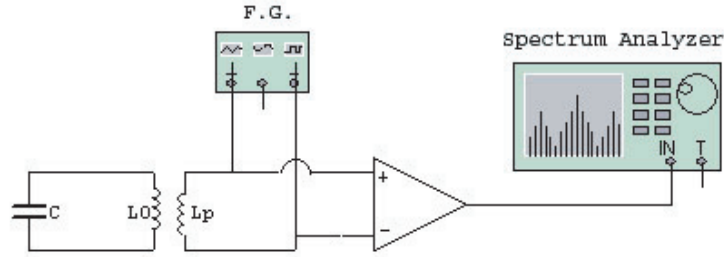


Figure 3.8: Experimental setup for the measurement of Q . F.G. is a function generator.

electrical mode was $\nu = (1170.94 \pm 0.01)$ Hz, in good agreement with the expected value. Then we excited the mode and observed the decay, shown in figure (3.9). Data points were acquired once every 30 seconds. The data have been fitted with an exponential decay of equation

$$y = A \cdot e^{\frac{-t}{\tau}} \quad (3.18)$$

We obtained for τ the value of 286.8 seconds, and thus from equation (3.15), we get $Q = 1.05 \cdot 10^6$.

But the transformer is not yet complete: it needs a secondary coil. As already stated, the value of L must be of the order of a few μH . This has been achieved by winding 3 turns of Nb wire, $125 \mu\text{m}$ thick, around the primary coil. In this case the predicted inductance is $1.5 \mu\text{H}$, while the measured value is $1.8 \mu\text{H}$ at room temperature and $1.3 \mu\text{H}$ at liquid helium temperature.

This secondary coil has been made to keep the coupling coefficient k of

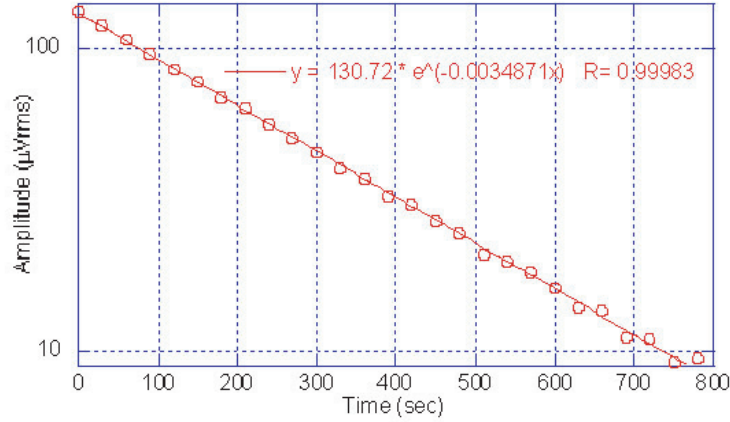


Figure 3.9: Decay of the electrical mode. Circles are the experimental data and the straight line is the fit.

the order of 0.40. We needed to do so, because it has been shown [64, 65] that a SQUID-high- Q resonator system is not stable. It is also possible to see that for a superconducting transformer, the coupling coefficient is given by

$$k = \sqrt{1 - \frac{L_1}{L_0}} \quad (3.19)$$

where L_1 and L_0 are the values of inductance of the primary coil when the secondary coil is short-circuited and open respectively. Since we measured $L_1 = 1.71$ H, and $L_0 = 2.09$ H, one has $k = 0.42$.

Now that the superconducting transformer has been fully characterized, we can integrate it with the other circuital components of the read-out chain.

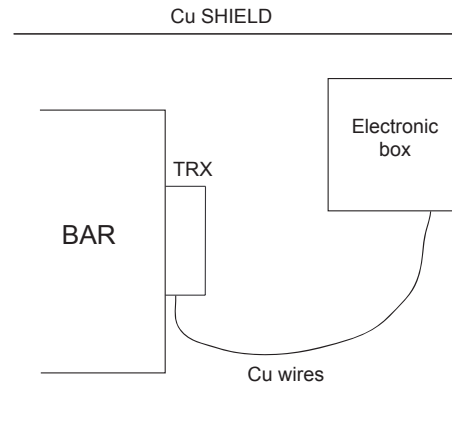


Figure 3.10: The position of the electronic box with respect to the bar and transducer (TRX).

3.3 The electronic box

All the electronic components of the read-out chain are housed in a box, screwed on the last Cu thermal shield, as shown in figure (3.10). To improve the thermal link between the components and the Cu shield, the box is made of Cu OFHC. Besides, to shield the components from external magnetic fields, the box has been plated with Sn40%Pb60%.

The box is composed of three separate chambers: one to house the superconducting transformer, another for the decoupling capacitor and the polarization resistances and the third for the SQUID. To avoid mechanical vibrations of the components, they are all firmly screwed on the box with an appropriate holder, different for each component. For instance, as can be seen from figure (3.11), the decoupling capacitor and the polarization resistances are screwed on a Teflon holder. We performed several

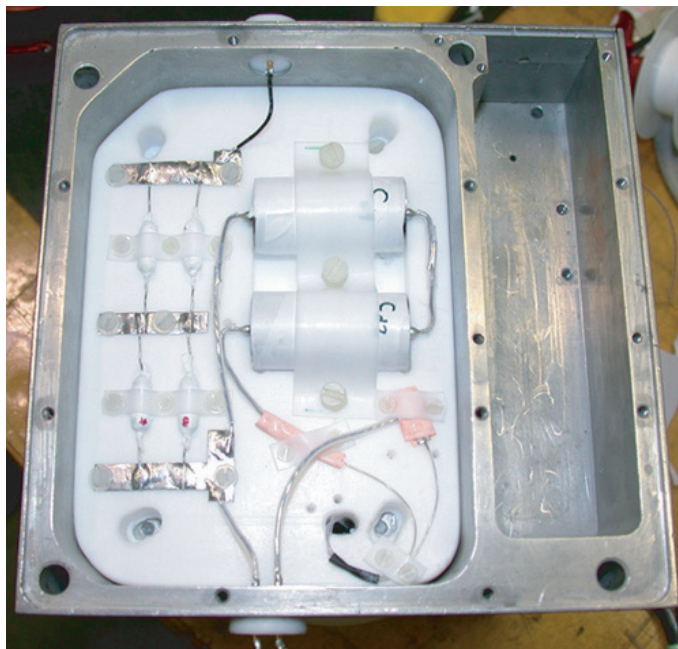


Figure 3.11: The electronic box. On the left it is possible to see the polarization resistances, while on the center of the picture we can see the decoupling capacitors and the contacts with the primary coil. The empty chamber on the right is that for the SQUID.

measurements, adding one component at a time, to study its influence on the electrical Q . The basic circuital scheme is that of figure (3.8).

As already stated in Section 3.1, the decoupling capacitor must fulfill the condition that $C_d \gg C_p + C_t$, so we used two commercial Teflon capacitors, of the same kind of that used for the Q measurements. These capacitors had measured capacitances of $C_{d_1} = 193$ nF and $C_{d_2} = 93$ nF at room temperature. They were connected in series, so that their total value at 4.2 K was $C_{series} = 64$ nF.

So we measured the Q of the LC circuit, where, now, C is the series of the capacitor simulating the transducer and the decoupling capacitors. The measurement was again performed observing the decay of the electrical mode. The result is that now $Q = 5.2 \cdot 10^5$. So the decoupling capacitors lower the Q by a factor of two.

The polarization resistances are directly connected to the transducer. We then chose high value resistors to filter all the possible disturbances. As in the past runs it happened that some of these resistors broke, we assembled them in a redundant configuration, building a series of two parallels. We used four resistors each with a measured resistance of $R_p = 5$ G Ω . As they are not directly in the read-out circuit, their influence on the electrical Q , should be, in principle, null. Anyway, we decided to verify this assumption. We built a parallel LCR circuit and, again, we measured the decay of the electrical mode. The measurement did not confirm our hypothesis, since we obtained $Q = 4.3 \cdot 10^5$. So the

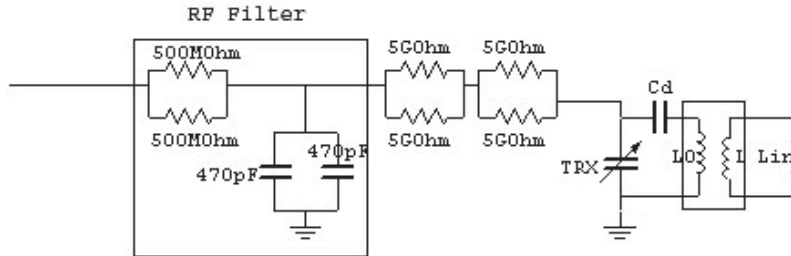


Figure 3.12: The complete scheme of the read-out electronics.

polarization resistances decrease the Q by more than a factor of two. This could be due to parasitic capacitance effects. We then added the complete charging line of the transducer, which is made, besides the polarization resistances, of a coaxial cryogenic cable⁷, made of NbTi in CuNi matrix, insulated with FORMVAR[®] and Teflon, and a radio-frequency filter. The complete scheme of the read-out circuit is shown in figure (3.12).

As can be seen from figure (3.10), when mounted on the detector, the transducer is connected to the electronic box via a pair of thin Cu wires, to avoid shortcircuiting the last stage of the mechanical suspensions. So we wanted to determine their influence on the electrical Q and what would be the difference if using Nb wires. The result is that in the case of Cu wires $Q = 1.4 \cdot 10^5$, while with Nb wires $Q = 2.2 \cdot 10^5$. Even if the Q is higher almost by a factor of two with Nb wires, we decided to use

⁷The cable has been bought from Leiden Cryogenics.

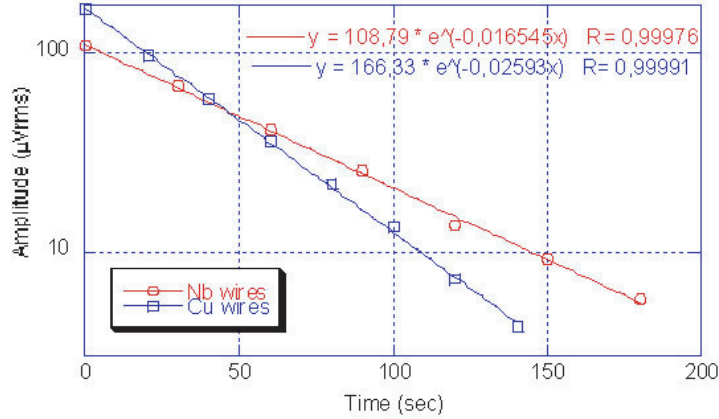


Figure 3.13: Comparison of the decay of the electrical mode when the transducer is connected to the electronic box via Cu or Nb wires. Circles and squares are the experimental data and the straight lines are the fit.

Cu wires in the final configuration, because the mechanical strength of thin ($50\ \mu\text{m}$) Nb wires is very poor.

All the measurements up to now have been performed keeping the secondary coil open. But in our final configuration, the secondary coil will be connected to the input inductance of the SQUID. So, to simulate this condition, we performed a Q measurement shortcircuiting the secondary coil. The short circuit was made with pressure contacts, since they have a critical current much higher than electrical discharge weldings. By solving the transformer equations, it is easy to see that when in the primary coil the current is i_1 and the secondary coil is closed on a generic

load Z , the current i_2 circulating in the coil is

$$i_2 = \frac{\omega k \sqrt{L_0 L}}{\sqrt{Z^2 + \omega^2 L^2}} i_1 \quad (3.20)$$

Since in our case $Z = 0$, the previous equation becomes

$$i_2 = k \sqrt{\frac{L_0}{L}} i_1 \quad (3.21)$$

and with our values of k , L_0 and L , we see that $i_2 \simeq 5 \cdot 10^2 i_1$. With this setup, we obtained $Q = 1.3 \cdot 10^5$.

We can then say that we succeeded in increasing the electrical Q by two orders of magnitude.

3.4 SQUID measurements

Before installing the electronic box on the detectors, a few checks must be done.

The secondary coil of the transformer is connected to the input coil of the SQUID via pressure contacts. It is crucial that these contacts are superconducting. Figure (3.14) shows the experimental setup used for this measurement. The idea is that when a constant magnetic flux is fed to the $L - L_{in}$ loop, a superconducting permanent current arises to cancel the effect of the external flux. The net effect is that a constant voltage arises across the SQUID. So the measurement consists in feeding

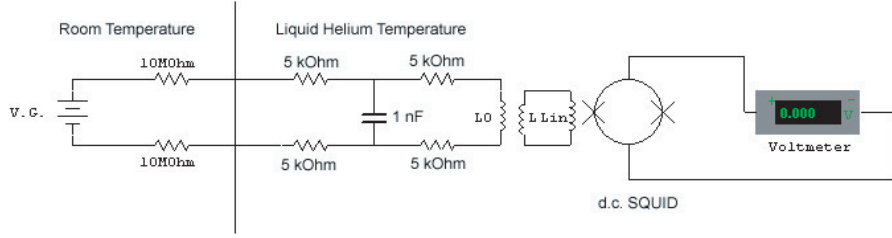


Figure 3.14: Scheme of the experimental setup for the measurement of the superconducting contacts. V.G. is a voltage generator. The resistances and the capacitor on the feed line are radio-frequency filters.

a constant voltage, of the order of 100 mV, to the $L - L_{in}$ loop, observing the output of the SQUID for some time (some minutes) and checking that this output is really a constant. The result of the measurement is shown in figure (3.15). The data can be fitted with an exponential decay, where the time constant τ is given by R/L , to obtain an upper limit on the resistance of the contacts. By doing so we obtained $R \leq 2.57 \cdot 10^{-12} \Omega$.

But the most important measurement is the one that verifies if the SQUID is working connected with a high- Q resonant circuit. In this case the scheme is that of figure (3.12). We noticed that the SQUID would lock quite easily and was very stable. We found the resonance of the electrical mode at $\nu_{el} = (1316.860 \pm 0.001) \text{ Hz}$, in very good agreement with the expected value of $\nu_{el} = 1322 \text{ Hz}$, given by the formula

$$\nu_{el} = \frac{1}{2\pi \sqrt{L_0 \left(1 - k^2 \frac{L_{in}}{L + L_{in}}\right) \left(\frac{C_{trx} C_d}{C_{trx} + C_d}\right)}} \quad (3.22)$$

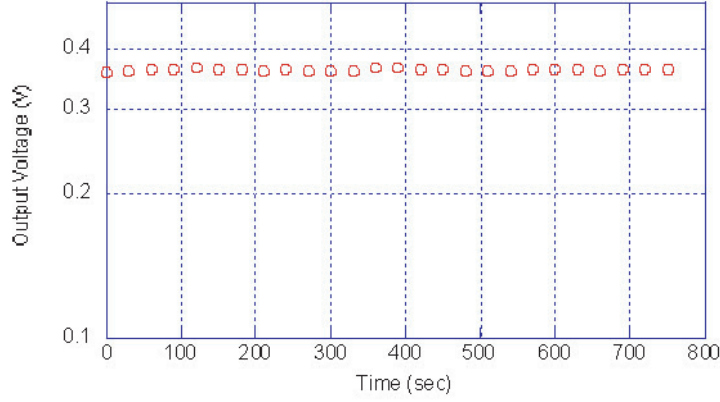


Figure 3.15: The measurement of the superconducting contacts. The vertical axis is the voltage across the SQUID and the horizontal axis is time in seconds.

The Q of the mode ranged from $2 \cdot 10^4$ to $3.7 \cdot 10^5$, deeply influenced by the working parameters of the SQUID. We also performed several noise measurements, obtaining, as the best result, $2.9 \cdot 10^{-5} \phi_0 / \sqrt{\text{Hz}}$. Since this value is a factor of ten worse than what it is possible to measure with the SQUID alone, we think this value is limited by the intrinsic noise of the cryostat.

3.5 Preliminary results of NAUTILUS 2003

The detector was reassembled during December 2002 and, after a month of pumping over the experimental and isolation vacuum, the cooling

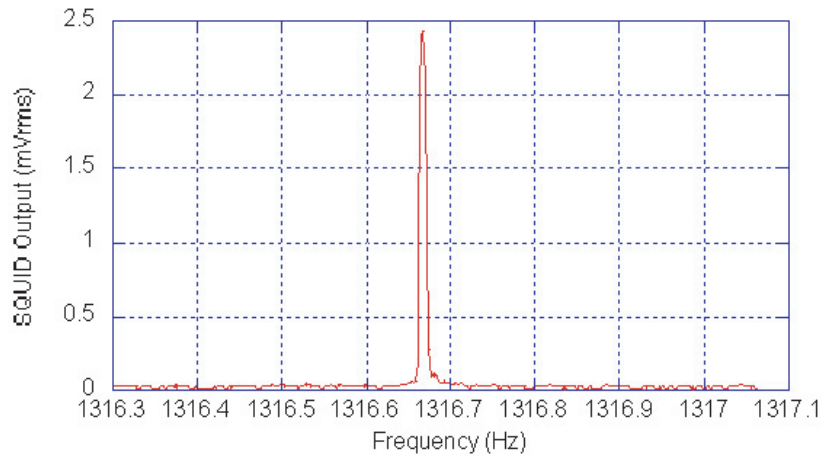


Figure 3.16: The peak resonance of the electrical mode as seen from the SQUID.

started in January 2003 and ended two months later.

Since the detector is totally new, starting from the bar itself, we decided not to turn on the dilution refrigerator. So now the thermodynamical temperature of NAUTILUS is 3.5 K, reached by pumping on the helium reservoir, which is kept below the superfluid transition, also to get rid of the extra noise due to the bubbling.

So we started the operations needed for optimal tuning and calibration of the detector. We chose the SQUID parameters in order to minimize the wide-band noise and to increase the stability.

Then the detector has been calibrated. Calibrations are made by exciting the detectors' modes with signals of known energy, via a PZT ceramic glued on the bar, and reading the output from the SQUID.

In the following we present the preliminary results obtained thanks to

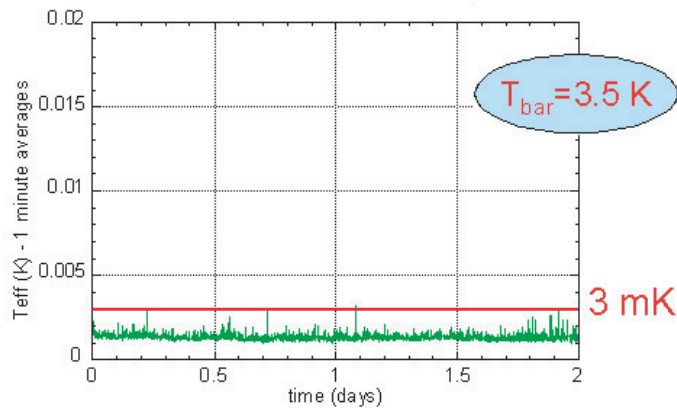


Figure 3.17: T_{eff} of NAUTILUS in June 2003. Units on the vertical axis are K.

the new read-out chain. Figure (3.17) shows the noise temperature T_{eff} of the detector over two days of June 2003 averaged over one minute.

As it can be seen from figure (3.17), the daily disturbances are not present anymore. So that the detector is sensitive 24 hours a day. This must be compared to figure (3.2). The most striking feature is that T_{eff} is constantly well below 3 mK, even if the thermodynamic temperature of the bar is higher than that of 2001 (1.5 K). This can also be seen by computing the distribution of T_{eff} in 2001 and 2003.

Figure (3.18) shows the distributions of T_{eff} of NAUTILUS in June 2003 (upper figure) and the whole 2001 (lower figure). To better compare the two results, we took out all the periods of cryogenic operations from the 2001 data. What is really evident is the decrease of T_{eff} from 3.5 mK to 1.3 mK. Furthermore, we must notice that the horizontal scales of the two distributions are very different. The scale of the distribution of the

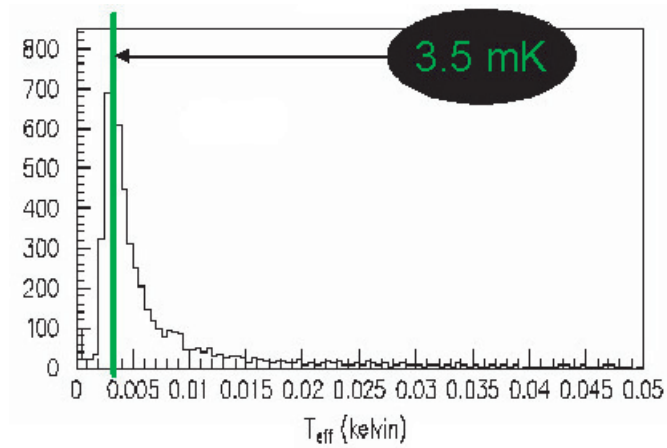
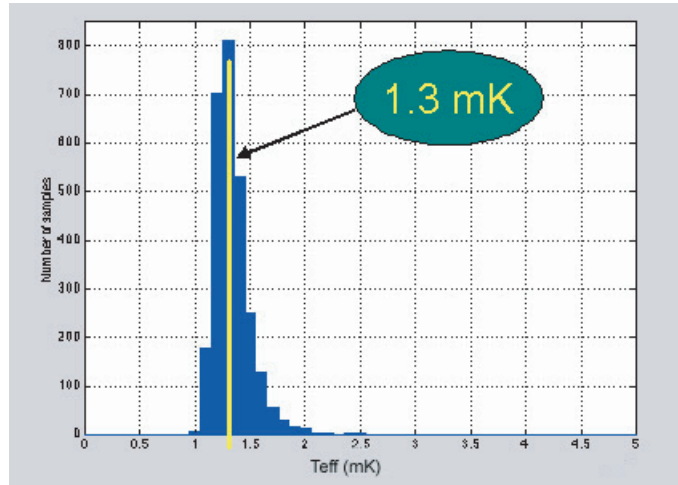


Figure 3.18: Distribution of T_{eff} of NAUTILUS in June 2003 (upper figure) and the whole 2001 (lower figure), where the periods of cryogenic operations have been taken out.

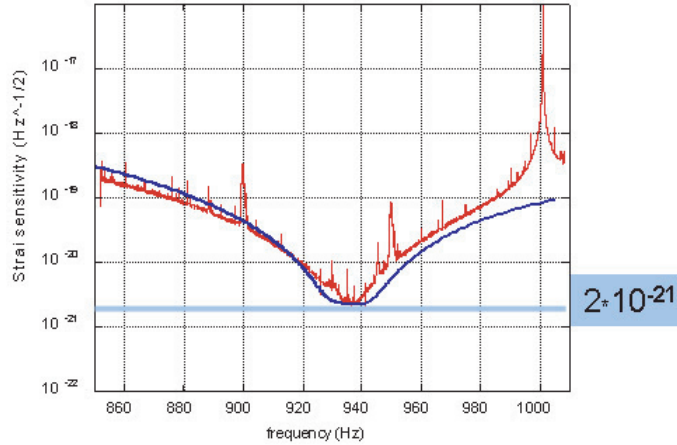


Figure 3.19: Experimental strain sensitivity of NAUTILUS in 2003 (red line) and GASP prediction (blue line).

2001 data goes from 0 to 50 mK, while that of the 2003 data ranges from 0 to 5 mK. This is another point that accounts for the better stability of the detector in 2003.

The decrease of T_{eff} is very important, since it is now possible to look for events with lower SNR.

Another way to look at the improvement of the NAUTILUS performances is to calculate the strain sensitivity reached in 2003, shown in figure (3.19). The figure shows both the experimental result (red line) and the prediction (blue line) of the GASP model [62]. The peak sensitivity is $2 \cdot 10^{-21} / \sqrt{\text{Hz}}$ at 935 Hz.

A direct comparison between figures (3.1) and (3.19) is impossible, since the bar temperature in 1999 was 0.15 K. But what is evident is

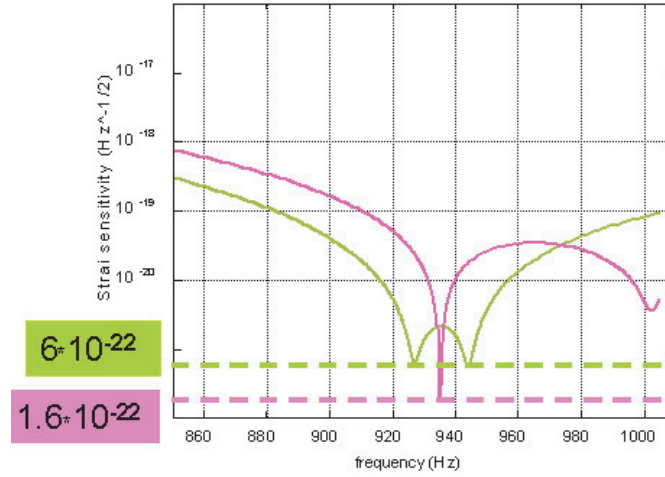


Figure 3.20: The expected strain sensitivity of NAUTILUS when cooled to 0.15 K.

that bandwidth of NAUTILUS 2003 has been increased by a factor of five, going from 6 Hz at the level of $10^{-20}/\sqrt{\text{Hz}}$ to more than 30 Hz at the same level. Since the agreement of the model to the experimental data is so good, we can compute the sensitivity of the detector when it will be cooled to 0.15 K. The result is shown in figure (3.20). The two curves only differ by the electric field stored in the transducer and they show the ability of the detector to work in both narrow-band and wide-band modes. In the first mode the peak sensitivity is $1.6 \cdot 10^{-22}/\sqrt{\text{Hz}}$ at 935 Hz, that would allow the detection of the GW from the pulsar 1987A integrating the signal for three months. While in the case of the wide-band mode, we can see that the bandwidth of the detector would be of the order of 60 Hz at the level of $10^{-20}/\sqrt{\text{Hz}}$.

At the moment of writing this thesis, no coincidence analysis or search for the pulsar have been performed yet.

Chapter 4

The d.c. SQUID

4.1 The Josephson junction

A Josephson junction is made by inserting a thin layer of insulating material between two superconducting elements. If the layer is thin enough, it is possible that Cooper pairs cross the potential well of the insulating material thanks to a tunneling effect. Picture (4.1) shows a scheme of a Josephson junction. We suppose that the superconductors $S_{1,2}$ are equal and that the junction be symmetric. We call $\psi_{1,2}$ the wave functions of the Cooper pairs in the two superconductors. They will decrease exponentially, but if the insulator is thin enough, they will penetrate enough to overlap. Then the total energy of the system will decrease. When the coupling energy becomes higher than the thermal fluctuations, the phases of the two wave functions are connected and the Cooper pairs

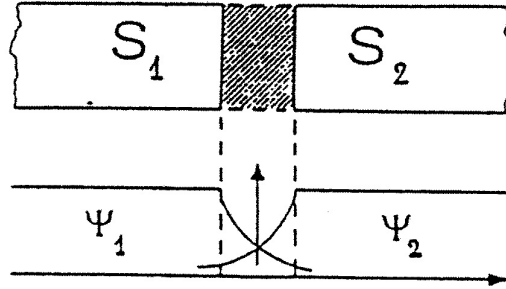


Figure 4.1: Scheme of a Josephson junction.

cross the junction without loosing energy. We will see that the tunneling of the pairs occurs even if there is an applied voltage to the junction: in this case the phases are not connected, but vary according to the applied voltage.

We can write the Schrödinger equations as [66]

$$\begin{aligned} i\hbar\dot{\psi}_1 &= U_1\psi_1 + K\psi_2 \\ i\hbar\dot{\psi}_2 &= U_2\psi_2 + K\psi_1 \end{aligned} \tag{4.1}$$

where $U_{1,2}$ are the energies in the fundamental state of the two superconductors, and K is the amplitude of the coupling. This parameter gives a measure of the interaction energy of the superconductors and depends on the nature and dimensions of the junction.

If we apply a voltage V across the junction, the fundamental state is translated by a quantity $e \cdot V$ and $|U_2 - U_1| = 2e \cdot V$. We define the zero

energy at half the junction so that equations (4.1) become

$$\begin{aligned} i\hbar\dot{\psi}_1 &= eV\psi_1 + K\psi_2 \\ i\hbar\dot{\psi}_2 &= -eV\psi_2 + K\psi_1 \end{aligned} \quad (4.2)$$

It is possible to show that putting $\psi_{1,2} = \sqrt{\rho_{1,2}}e^{i\theta_{1,2}}$, where ρ is the density of the Cooper pairs and θ is the phase, and separating the imaginary and real parts, we get

$$\begin{aligned} \dot{\rho}_1 &= \frac{2}{\hbar}K\sqrt{\rho_1\rho_2}\sin\delta \\ \dot{\rho}_2 &= -\frac{2}{\hbar}K\sqrt{\rho_1\rho_2}\sin\delta \end{aligned} \quad (4.3)$$

and

$$\begin{aligned} \dot{\theta}_1 &= \frac{K}{\hbar}\sqrt{\frac{\rho_1}{\rho_2}}\cos\delta + \frac{eV}{\hbar} \\ \dot{\theta}_2 &= \frac{K}{\hbar}\sqrt{\frac{\rho_1}{\rho_2}}\cos\delta - \frac{eV}{\hbar} \end{aligned} \quad (4.4)$$

where $\delta = \theta_1 - \theta_2$ is the phase between the two superconductors. The current density is $J = \rho_1 = -\rho_2$. By using equation (4.3), becomes:

$$J = \frac{2}{\hbar}K\sqrt{\rho_1\rho_2}\sin\delta \quad (4.5)$$

If we assume that $\rho_1 = \rho_2 = \rho_c = \text{constant}$, we can write the previous equation as:

$$J = J_c \sin\delta \quad (4.6)$$

where we defined $J_c = 2K\rho_c/\hbar$. If K is constant over all the surface S of the junction, then $I_c = J_c S$ is the critical current of the junction. This current depends on many factors, but a way to define a good junction is

that I_c weakly depends on the temperature when $T < T_c$.

We must notice that, even if the density of Cooper pairs is constant, its time derivative is non zero. From equations (4.4) we obtain

$$\dot{\delta} = \frac{2eV}{\hbar} = 2\pi \frac{V}{\phi_0} \equiv \omega_J \quad (4.7)$$

and it follows that

$$\delta(t) = \delta_0 + \frac{2e}{\hbar} \int V(t) dt \quad (4.8)$$

where we indicated with δ_0 the value of the phase for $t = 0$.

Equation (4.6) and (4.7) completely describe the Josephson effect.

If $V = 0$, then δ is constant, so across the junction flows a current even if there is no applied voltage. This is the DC Josephson effect.

When $V \neq 0$, we can see from equations (4.6) and (4.8) that AC currents are present

$$J = J_c \sin \left(\delta_0 + \frac{2eV}{\hbar} t \right) \quad (4.9)$$

The quantity $\nu_J = \frac{2eV}{\hbar} = \frac{V}{\phi_0}$ is called *Josephson frequency* and

$$\frac{\nu_J}{V} = 483.6 \text{ MHz}/\mu\text{V} \quad (4.10)$$

This is the AC Josephson effect.

Figure (4.2) shows the $I - V$ characteristics of a Josephson junction current polarized. It is possible to see a hysteresis effect: for polarization

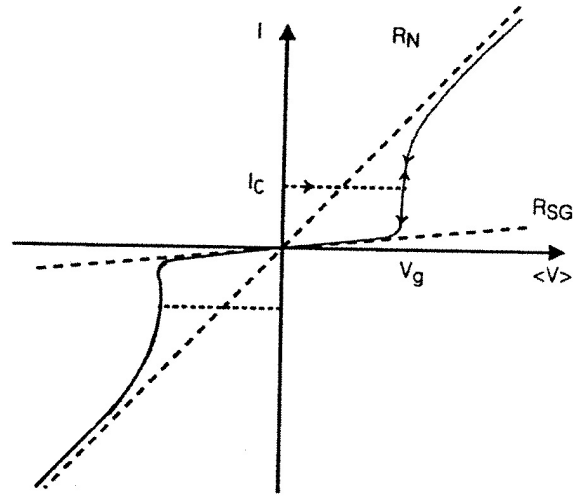


Figure 4.2: $I - V$ curve of a Josephson junction.

currents $|I| < I_c$, the voltage across the junction is zero, a supercurrent flows due to the tunneling of Cooper pairs; as soon as $|I| > I_c$, a voltage appears across the junction¹; increasing the current, the voltage increases and the curve tends to the line $I = V/R_n$. When the current is decreased below I_c , the voltage does not disappear immediately, but goes down along the curve and becomes zero only if $|I| \ll I_c$. The part of the curve corresponding to $|V| < 2\Delta/e$ can be approximated with a line of slope $1/R_{SG}$ and represents the current due to the electrons in the normal part of the electrodes due to the impurities and, at $T \neq 0$, to the tunneling of quasi-particles.

¹Measurements show that $|V_g| > 2\Delta/e$, where Δ is the value of the gap in the BCS Theory.

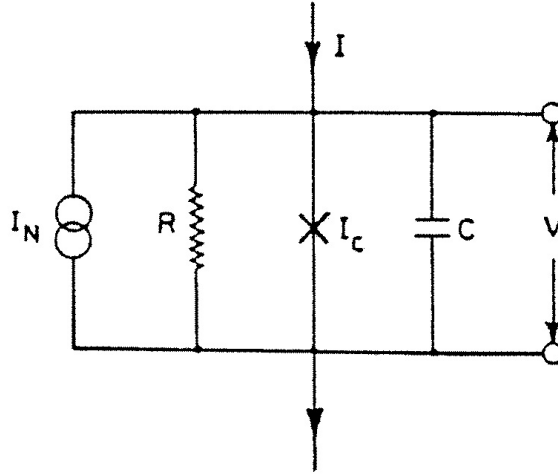


Figure 4.3: Model of a resistively *shunted* junction.

4.2 RSJ model

The hysteresis effect of a Josephson junction is usually an unwanted characteristic on a SQUID. This problem can be solved by inserting in parallel to the junction an appropriate resistance, called *shunt* (Mc Cumber, 1968; Stewart, 1968). Figure (4.3) shows a model of a shunted junction. Beside the shunt resistance, there is a current noise generator $I_N(t)$, connected with this resistance, the capacity of the junction and a tunneling element with critical current I_c . The circuit equations, neglecting the noise contribution, are

$$\frac{V}{R} + I_c \sin \delta + C\dot{V} = I \quad (4.11)$$

where I is the applied current and

$$V = \frac{\hbar \dot{\delta}}{2e} \quad (4.12)$$

By replacing equation (4.12) into (4.11) we obtain

$$\frac{\hbar C}{2e} \ddot{\delta} + \frac{\hbar}{2eR} \dot{\delta} = I - I_c \sin \delta \quad (4.13)$$

that we can rewrite in adimensional way

$$\beta_c \frac{d^2 \delta}{d\tau^2} + \frac{d\delta}{d\tau} = i - \sin \delta \quad (4.14)$$

by defining the following quantities

$$\begin{aligned} \beta_c &= \frac{2\pi I_c R^2 C}{\phi_0} = \omega_J R C \\ \tau &= \frac{t}{\phi_0 / 2\pi I_c R} = \omega_J t \\ i &= \frac{I}{I_c} \end{aligned} \quad (4.15)$$

The quantity i is called reduced current, while for the *Josephson frequency* one has

$$\frac{\omega_J}{2\pi} = \frac{2eV}{2\pi\hbar} = \frac{2eI_c R}{h} \quad (4.16)$$

Equation (4.14) can only be solved numerically, but if I is constant and $\beta_c \ll 1$, an analytical solution can be found [67]

$$\delta(t) = 2 \tan^{-1} \left[\sqrt{\frac{i^2 - 1}{i^2}} \tan \frac{\pi t}{T} - i \right] \quad (4.17)$$

where

$$T \propto \frac{2\pi}{\omega_J} \left[\frac{I}{I_c} \right]^{-\frac{1}{2}} \quad (4.18)$$

is the oscillation period. From equation (4.17), it is possible to study the behaviour of the voltage since

$$V(t) = \frac{\hbar}{2e} \dot{\delta} \quad (4.19)$$

As for polarization currents higher than the critical current, $T \simeq 1$ ns, the junction behaves as a voltage oscillator, with frequency equal to the Josephson frequency and amplitude proportional to the average voltage [67]

$$\langle V \rangle = \frac{\hbar}{2eT} \int_0^T \dot{\delta}(t) dt = I_c R \sqrt{\left(\frac{I}{I_c} \right)^2 - 1} \quad (4.20)$$

Figures (4.4) and (4.5) show the behaviour of equations (4.19) and (4.20) for different values of I/I_c and $\beta_c = 0$. From the analysis of the figures it is possible to state the following:

- if $I < I_c$, in the junction flows a constant supercurrent and $\langle V \rangle = 0$;
- if $I \geq I_c$, a voltage, given by periodic pulses of frequency ν_J , arises

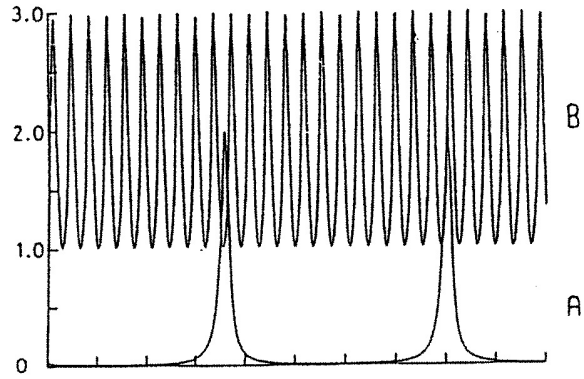


Figure 4.4: Behaviour of the output voltage (in units of $I_c R$) as a function of time for two values of I/I_c with $\beta_c = 0$.

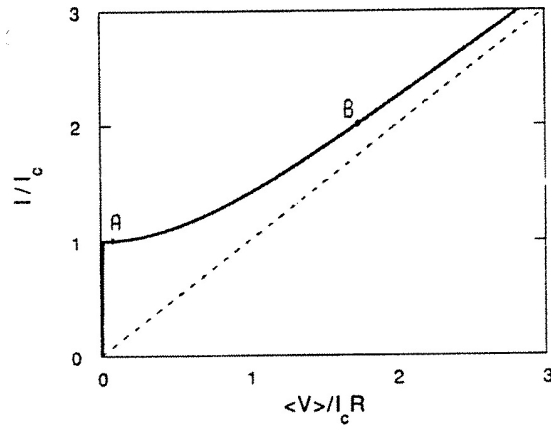


Figure 4.5: $I - V$ characteristic of a SQUID with $\beta_c = 0$.

across the junction;

- if $I > I_c$, the voltage across the junction is given by an oscillating term with zero average, superimposed to a constant signal that represents the contribution of the normal currents.

In general, if $\beta_c > 1$, the characteristic of the junction is hysteretical. In this case if $I < I_c$, two states are possible: $V = 0$ and $V \neq 0$. For this reason, only junctions with $\beta_c < 1$ are used in a SQUID.

4.3 The d.c. SQUID

A d.c. SQUID is realized by cutting a superconducting ring with two identical symmetrical Josephson junctions, both shunted to eliminate the hysteresis phenomenon. Figure (4.6) shows the schematic of a SQUID [68]: L is its inductance, I_c is the critical current, R and C the resistance and capacity of the shunt. A d.c. SQUID is polarized via a constant current I_b , in such a way that the currents flowing in the two branches are $I_b = I_1 + I_2$, where currents $I_{1,2}$ are functions of the voltages $V_{1,2}$ and of the phase differences across the junctions

$$I_{1,2} = I_c \sin \delta_{1,2} + \frac{V_{1,2}}{R} + C\dot{V}_{1,2} \quad (4.21)$$

We define the total current in the SQUID as

$$J = \frac{I_1 - I_2}{2} \quad (4.22)$$

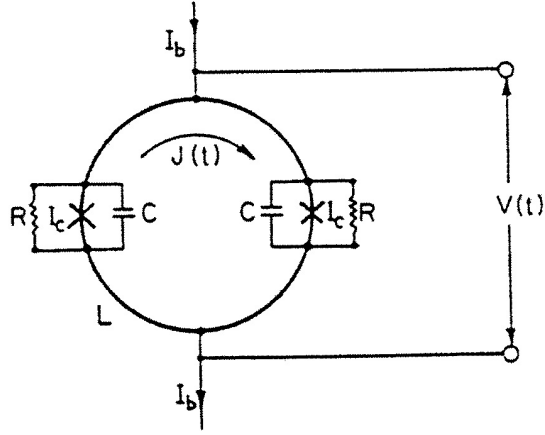


Figure 4.6: Circuital scheme of a d.c. SQUID

The phases and the voltages are connected by the second Josephson equation:

$$\dot{\delta}_{1,2} = \frac{2e}{\hbar} V_{1,2} \quad (4.23)$$

So, the voltage across the SQUID becomes:

$$\begin{aligned} V &= V_1 L_1 \dot{I}_1 + M \dot{I}_2 \\ &= V_2 L_2 \dot{I}_2 + M \dot{I}_1 \end{aligned} \quad (4.24)$$

where we used $L_{1,2}$ as the self inductances of the two branches of the SQUID and M is their mutual inductance. The phase difference are bound to the flux quantization condition

$$\delta_1 - \delta_2 = \frac{2\pi\Phi}{\phi_0} \quad (4.25)$$

Φ is the total flux linked to the SQUID, given by the sum of the external flux and that associated to the current J , $\Phi = \Phi_{ext} + LJ$.

If we consider the simplified case, where the shunt resistor, the self inductance of the ring and the capacity of the junctions are negligible. We then put $R = 0$, and since $L = 0$

$$\beta_L = \frac{2LI_c}{\phi_0} = 0 \quad (4.26)$$

furthermore $C = 0 \implies \beta_c = 0$, with β_c given from equation (4.15) Thus equations (4.21) become

$$I_{1,2} = I_c \sin \delta_{1,2} \quad (4.27)$$

and thus:

$$I_b = I_c(\sin \delta_1 + \sin \delta_2) \quad (4.28)$$

Since $L = 0$, it follows that $\Phi = \Phi_{ext}$ and so $\delta_1 - \delta_2 = 2\pi \frac{\Phi_{ext}}{\phi_0}$. We can rewrite equation (4.28) as

$$I_b(\Phi_{ext}, \delta_1) = I_c \sin \delta_1 + I_c \sin \left(\delta_1 - 2\pi \frac{\Phi_{ext}}{\phi_0} \right) \quad (4.29)$$

Maximizing with respect to δ_1 , we find that the critical current depends on the external flux in the following way

$$I_{cS}(\Phi_{ext}) = 2I_c \left| \cos \pi \frac{\Phi_{ext}}{\phi_0} \right| \quad (4.30)$$

From the previous equation it is clear that the critical current is modulated by the external flux. We note that the critical current varies from 0 to $2I_c$ for $(2N - 1)\frac{\phi_0}{2} \leq \Phi_{ext} \leq N\phi_0$. If we consider a dissipative term, with $\beta_c = \beta_L = 0$, $R \neq 0$ and $I_b = \text{constant}$, summing equations (4.21) we obtain two equations from which it is possible to obtain the output voltage of a d.c. SQUID

$$I_b = I_{cS} \sin \varphi + \frac{\hbar}{eR} \dot{\varphi} \quad (4.31)$$

and

$$V(t) = \frac{\hbar}{2e} \dot{\varphi} \quad (4.32)$$

where $\varphi = \delta_1 - \delta_2$. Equation (4.31) formally similar to (4.13), from which we obtained the behaviour of a single Josephson junction with $\beta_c = 0$. So we can extend the observations done on $\delta(t)$ to $\varphi(t)$. The solution of equation (4.31) is oscillating with period

$$T \propto \frac{2\pi}{\omega_J} \left[\left(\frac{I_b}{I_{cS}} \right)^2 - 1 \right]^{-\frac{1}{2}} \quad (4.33)$$

and the average voltage is given by

$$\langle V \rangle = \begin{cases} \frac{R}{2} \sqrt{I^2 - I_{cS}^2(\Phi_{ext})} & \text{if } |I_b| > I_{cS}(\Phi_{ext}) \\ 0 & \text{if } 0 \leq |I_b| \leq I_{cS}(\Phi_{ext}) \end{cases} \quad (4.34)$$

When the external flux is zero, the phase difference is zero and the

SQUID behaves as if it was a single junction with a critical current equal to the double of the critical current of each junction. If $\Phi_{ext} \neq 0$, the currents are out of phase. If $\Phi_{ext} = N\phi_0$ then the phase difference is an integer multiple of 2π and the junctions oscillate in phase, otherwise the phase shift is maximum. In this case the supercurrents interfere destructively, no critical current exists and the SQUID behaves as a resistor. In equation (4.21) the terms in $\sin(\delta)$ become zero and the equation reduces to

$$I = \frac{2V}{R} \quad (4.35)$$

where we used $R/2$ to indicate the parallel of the two shunt resistances.

We can then summarize the behaviour of a SQUID in the following way: a change of the linked flux, causes a change of the critical current, that, in its turn, causes a change both of the oscillation period of the voltage across the SQUID and of the average of this voltage. We must take in to account, that this voltage is the sum of two terms: a supercurrent that arises because of the AC Josephson effect when we polarize the SQUID with a current higher than I_{cS} , and a normal current that arises to keep the total current constant. Both these contributions oscillate at the same frequency with average values different from zero and cause a voltage with average value non zero.

If $R, L, C \neq 0$, calculations become somewhat more difficult [69], but it can be shown that the behaviour of a real d.c. SQUID is not much different from the ideal one. The only difference is that the minimum

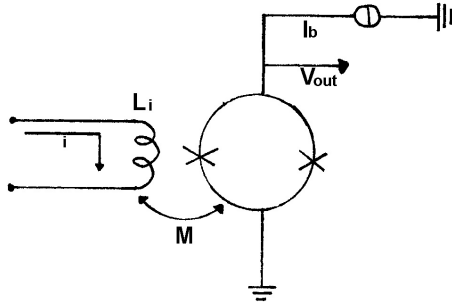


Figure 4.7: Input coil-SQUID system.

value of the critical current is not zero anymore, but, as Φ_{ext} varies, it depends on β_L .

4.4 The SQUID as an amplifier

In the GW research field, the d.c. SQUID is used as a current low noise amplifier. To do so, it is necessary to couple to the SQUID a coil that converts the current in magnetic flux. It is possible to draw the behaviour of the SQUID as a current amplifier in the following way

$$\delta i \Rightarrow \delta \phi_s = M \delta i = \frac{\partial V}{\partial \phi} \delta \phi_s = \frac{\partial V}{\partial \phi} M \delta i \quad (4.36)$$

A variable current flowing in the input coil, causes changes of the flux ϕ_s in the superconducting ring. This changes of ϕ_s cause, at the output of the SQUID, a variable voltage proportional to the input current. Because of the very high sensitivity of the SQUID, any external flux, coupled to

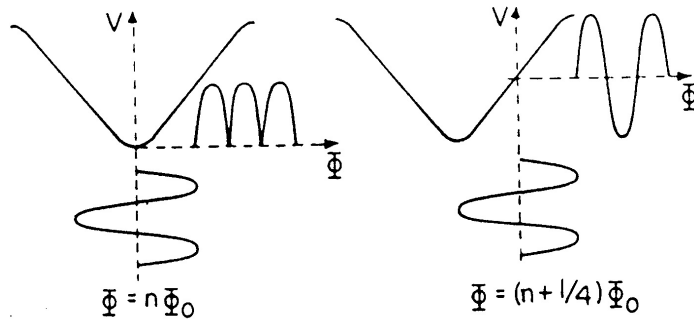


Figure 4.8: V_{out} produced by a modulating flux in different polarization conditions.

the input coil or to the SQUID itself, would change the working point and the responsivity of the SQUID. The solution is to make use of a feedback network to stabilize the working point and linearize the characteristics. Picture (4.8) shows that the output voltage of a SQUID is proportional to an external field, at the frequency of a modulation signal, that is sent back to the SQUID to keep the working point at $\phi_{ext} = n\phi_0$, where the $V - \phi$ characteristics are linear and $\partial V/\partial\phi$ is maximum. It is, thus, clear that to measure the flux changes it is necessary to send to the SQUID, via an appropriate coil, a modulation flux at the frequency ν_{mod} , with peak-to-peak amplitude of $\approx \phi_0/2$. From picture (4.8) we can see that if the total flux is an integer multiple of ϕ_0 , then V_{out} has a big component at the frequency $2\nu_{mod}$, while if the flux increases, the amplitude of the output signal of the SQUID increases at the frequency ν_{mod} . Increasing again the flux, the signal goes back at the frequency $2\nu_{mod}$, but with opposite phase. Picture (4.9) shows a typical read-out scheme of a SQUID [70].

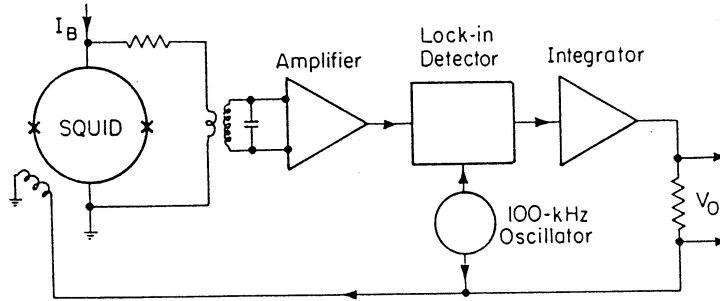


Figure 4.9: Modulation and feedback network for a d.c. SQUID.

The output signal from the SQUID is sent to a LC integrator circuit, resonating at ν_{mod} and acting as an impedance matching between the output impedance of the SQUID and the input impedance of the amplifier at room temperature. The output of the amplifier is then sent to a lock-in, that demodulates the signal at ν_{mod} . If the static flux coupled to the SQUID is an integer multiple of ϕ_0 , the output signal will be at $2\nu_{mod}$, and the lock-in output will be zero. Otherwise, if the flux equals $(n + \frac{1}{4})\phi_0$, the frequency of the output signal will be ν_{mod} and the lock-in output will be maximum.

The SQUID is an extremely sensitive device, capable of revealing magnetic fields of the order of 10^{-14} Tesla. So to shield external fields slowly varying, that could induce it to work in a saturation or non-linear regime, the SQUID is usually housed in a box, made of superconducting material. Besides, it has been proved that a SQUID must be shielded from radio-frequency noise, since this can lower its responsivity.

Chapter 5

The read-out of MiniGRAIL

As already said in Section 1.2.2, in Leiden, Holland, a spherical detector is being built. The sphere is made of CuAl6%, with a diameter of 65 cm, the mass is 1150 kg and the resonance frequency is around 3160 Hz (see figure 5.1). Thanks to an agreement between the Leiden and the Rome groups, the detector will be equipped with a read-out chain similar to that used on EXPLORER and NAUTILUS. Before equipping the detector with a complete read-out chain, we performed a measurement to characterize the overall noise of the antenna.

The next run of MiniGRAIL is expected to start in the second half of December 2003.



Figure 5.1: The MiniGRAIL detector. The picture shows the last stages of suspension system and of the dilution refrigerator.

5.1 Noise measurement with a PZT transducer

The calculations that follow, can be applied to any geometry resonant detector. It is possible to see [4] that a resonant antenna mode of effective mass m at a temperature T is subject to a brownian noise of energy $kT = m\omega_0^2\overline{\xi_0^2}$, where ξ_0 is the displacement of the antenna and T the temperature of the quadrupole mode. As already stated in Section 2.1.2, this temperature is in fact higher than the thermodynamic temperature, because of back-action and brownian noises (see equation (2.9)), and will be later indicated by T_e . In comparison with a bar detector, a spherical antenna at the same thermodynamical temperature has (potentially) a brownian displacement 3.4 times smaller. We describe here some preliminary measurements of the temperature of the quadrupole modes of MiniGRAIL, using a piezoelectric transducer (PZT).

5.1.1 The equivalent circuit

We will give a brief review of the noise sources involved in the experiment. It can be shown [71, 72] that a mechanical oscillator can be represented by an equivalent electrical RLC circuit, since the equations involved are formally identical. We assume that the mass of the PZT is negligible with respect of that of the antenna m . The output voltage of the PZT is

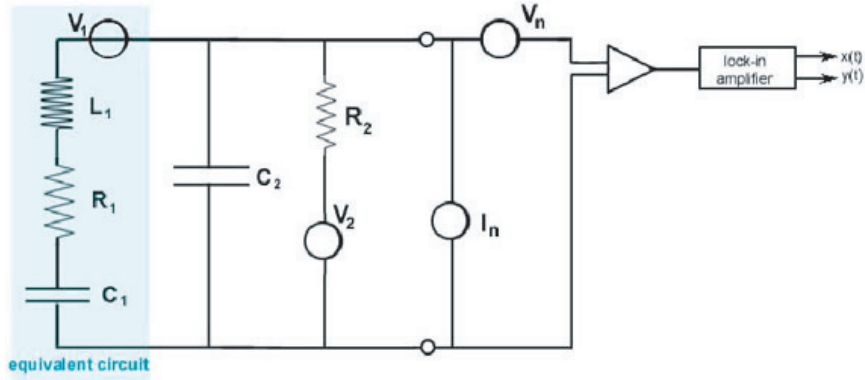


Figure 5.2: The equivalent circuit of the mode and the PZT with a FET amplifier. The noise sources of the FET amplifier are represented by I_n and V_n , while the electrical dissipations of the PZT are represented by R_2 , with a voltage noise source equal to V_2 .

related to the displacement of the surface of the sphere by the equation

$$V(t) = \alpha\xi(t) \quad (5.1)$$

and the equivalent parameters of the sphere-PZT system are defined as follows

$$\begin{aligned} L_1 &= \frac{m}{\alpha^2 C_2^2} \\ R_1 &= \frac{\omega_0 m}{2Q} \frac{1}{\alpha^2 C_2^2} \\ C_1 &= \frac{1}{L_1 \omega_0^2} = \frac{\alpha^2 C_2^2}{\omega_0^2 m} \end{aligned} \quad (5.2)$$

where C_2 is the capacitance seen at the output of the amplifier and includes the capacitance of the PZT, that of the cable and that of the amplifier. Figure (5.2) shows the equivalent circuit and all the noise

sources.

5.1.2 Noise sources of the system

The resistances R_1 and R_2 introduce noise in the circuit (Johnson noise) with spectral density

$$V_i^2 = 2kTR_i \left[\frac{\text{V}^2}{\text{Hz}} \right] \quad (5.3)$$

The other noise sources are given by V_1 , V_2 and those of the amplifier.

- The noise contribution of the voltage generator V_1 , due to the brownian motion of electric charges and phonons in the antenna, is represented by R_1 . Its power spectrum is given by

$$S_1(\omega) = V_1^2 |T_1(\omega)|^2 \quad (5.4)$$

where $T_1(\omega)$ is the transfer function given by

$$T_1(\omega) = \frac{1}{L_1 C_1} \frac{1}{\left(\omega_r^2 - \omega^2 + \frac{\omega}{\tau_0} \tan \delta \right) + i \left(\frac{\omega}{\tau_0} + (\omega^2 - \omega_0^2) \tan \delta \right)} \quad (5.5)$$

where τ_0 is the decay time of the mode and

$$\omega_r^2 = L_1^{-1} (C_1^{-1} + C_2^{-1}) = \omega_0^2 \frac{1}{1 - \beta} \quad (5.6)$$

The $\tan(\delta)$ term represents the electrical losses of the PZT. The transfer function $T_1(\omega)$ has a maximum for $\omega \simeq \omega_0$. The average

square value of the output voltage is given by

$$V_b^2 = \int_{-\infty}^{\infty} S_1(\omega) \frac{d\omega}{2\pi} = \frac{2\alpha^2 kT}{m\omega_r^2} \quad (5.7)$$

- The noise voltage V_2 is caused by the electrical dissipations in the PZT, and can be represented by a current noise generator in parallel to R_2 equal to $I_2 = V_2/R_2$. This generator sees an impedance

$$Z(\omega) = \frac{R_1 + i\omega L_1 + (i\omega C_1)^{-1}}{i\omega C_2(1 - i \tan \delta) [R_1 + i\omega L_1 + (i\omega C_1)^{-1} + (i\omega C_2(1 - i \tan \delta))^{-1}]} \quad (5.8)$$

and thus brings a contribution to the output voltage spectral density equal to

$$\int_{-\infty}^{\infty} |Z(\omega)|^2 I_2^2 \frac{d\omega}{2\pi} = \frac{QC_1^2}{2\omega_r C_2^4} I_2^2 + \int_{-\infty}^{\infty} \frac{I_2^2}{\omega^2 C_2} \frac{d\omega}{2\pi} \quad (5.9)$$

Which is a sum of a narrow-band and a wide-band contribution. The first term can be calculated for $\omega \simeq \omega_r$.

$$V_2^2 = \frac{QC_1^2 \tan \delta}{C_2^3} kT [\text{V}^2] \quad (5.10)$$

While the wide-band term has a spectral density

$$S_2 = \frac{2kT \tan \delta}{\omega C_2} \left[\frac{\text{V}^2}{\text{Hz}} \right] \quad (5.11)$$

- The current noise source of the amplifier I_N generates a noise that

is identical to that obtained for I_2 , since it is in parallel with R_2 and sees the same impedance. So the narrow-band noise amplitude is

$$V_{Nn}^2 = \frac{QC_1^2}{2\omega_r C_2^4} I_N^2 \text{ [V}^2\text{]} \quad (5.12)$$

and the wide-band spectral density is again given by an equation equal to (5.11)

$$S_N = \frac{2kT \tan \delta}{\omega C_2} \left[\frac{\text{V}^2}{\text{Hz}} \right] \quad (5.13)$$

The voltage noise of the amplifier V_N is simply added quadratically to the other wide-band noises. The total narrow-band noise is then given by

$$V_{nb}^2 = \frac{2\alpha^2 kT}{m\omega_r^2} \left(1 + \frac{\beta Q I_N^2}{2\omega_r C_2 kT} \right) \quad (5.14)$$

This noise can be seen as a pure brownian noise at a temperature T_e larger than the thermodynamic temperature T . The increase in temperature is mainly due to the back-action of the current noise of the amplifier. We can then write

$$V_{nb}^2 = \frac{2\alpha^2 kT_e}{m\omega_r^2} \quad (5.15)$$

where

$$T_e = T \left(1 + \frac{Q\beta I_N^2}{2\omega_r C_2 kT} \right) \quad (5.16)$$

The total wide-band noise spectral density is given by

$$V_0^2 = V_N^2 + \frac{2kT \tan \delta}{\omega C_2} + \frac{I_N^2}{\omega^2 C_2^2} \quad (5.17)$$

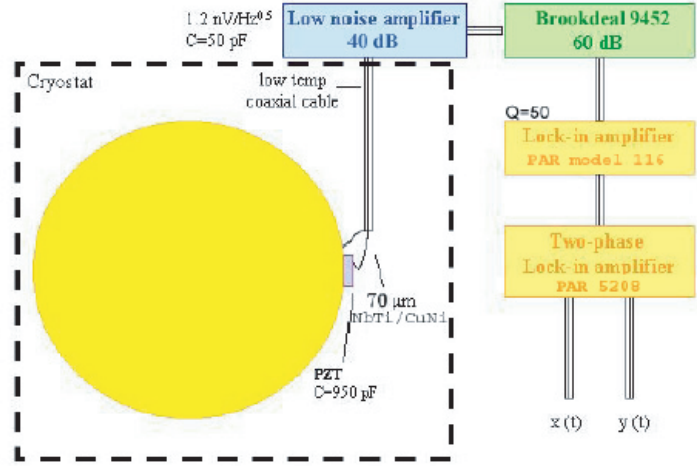


Figure 5.3: The scheme of the measuring setup.

5.1.3 Measurement of T_e

Picture (5.3) shows the experimental setup for the measurement. A low noise amplifier directly reads the output of the PZT, then the signal is furtherly amplified and sent to a two-phase lock-in. The lock-in outputs $x(t)$ and $y(t)$ can be seen as the real and imaginary components of the Fourier transform of $V(t)$ at ω_s

$$\begin{aligned}
 x(t) &= \frac{1}{t_0} \int_{-\infty}^t V(t') e^{-\frac{(t-t')}{t_0}} \text{sign}(\cos \omega_s t') dt' \\
 y(t) &= \frac{1}{t_0} \int_{-\infty}^t V(t') e^{-\frac{(t-t')}{t_0}} \text{sign}(\sin \omega_s t') dt'
 \end{aligned} \tag{5.18}$$

These quantities were acquired on a PC by a LabView program. Than, on a different PC, another LabView program would perform the on-line analysis. The outputs of the lock-in amplifier were used to build the

quantity

$$r^2(t) = x^2(t) + y^2(t) \quad (5.19)$$

It can be shown [4] that r^2 has a Gaussian distribution

$$F(r^2) = \frac{1}{2\sigma_0^2} e^{-\frac{r^2}{2\sigma_0^2}} \quad (5.20)$$

where σ_0 is the variation of the distribution of the signal at the output of the lock-in amplifier. This variation is the sum of narrow-band and wide band terms

$$\sigma_0^2 = V_{nb}^2 + \frac{S_0^2}{t_0} \quad (5.21)$$

where t_0 is the lock-in integration time.

So, the on-line data analysis program (see figure (5.4)), computes r^2 and shows the real-time behaviour of r^2 versus time. Besides it computes the histogram of r^2 and performs a fit to evaluate T_e . The slope of the histogram is $-1/2\sigma_0$, since in our case $S_0^2 \ll V_{nb}^2$, from equation (5.15) it turns out that T_e is given by the formula

$$T_e = \frac{C_2}{k\beta} V_{nb}^2 \quad (5.22)$$

To evaluate β , the PZT must be calibrated. This calibration can be done using the equivalent circuit of the mode of interest. A known amount of energy is fed to the mode, by exciting the PZT with a known voltage V_g , for a time short compared to the decay time of the mode. In

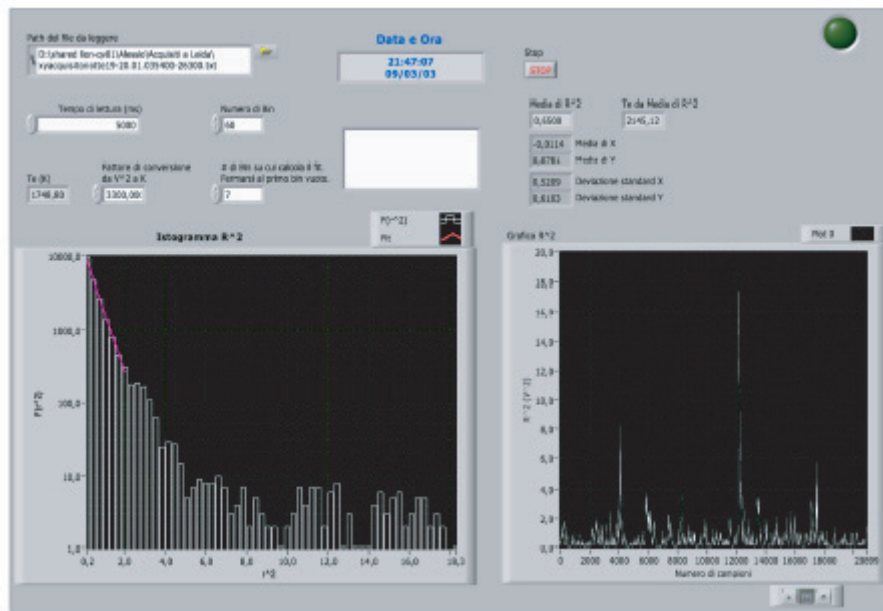


Figure 5.4: Control Panel of the on-line analysis program. The plot on the left is the histogram of r^2 , while that on the right shows the real-time behaviour of r^2 versus time. The plot refers to 6 hours of data acquisition.

this way we can estimate C_1 from the equation

$$C_1 = \frac{V_0 C_2}{V_g \Delta t \pi f_0} \quad (5.23)$$

where V_0 is the output voltage from the PZT at $t = 0$ (time when the excitation was stopped and the decay started) and f_0 is the resonance frequency of the mode. Then we can define

$$\beta = \frac{\frac{1}{2} C_2 V_2^2}{\frac{1}{2} C V} \quad (5.24)$$

the ratio between the energy stored in the PZT and that stored in the mode. Since

$$C = \frac{C_1 C_2}{C_1 + C_2} \text{ and } V_2 = \frac{C_1}{C_1 + C_2} V \quad (5.25)$$

we get

$$\beta = \frac{C_1}{C_1 + C_2} \simeq \frac{C_1}{C_2} \quad (5.26)$$

In our case we had $C_2 = (950 \pm 50)$ pF, $C_1 = 3.7 \cdot 10^{-17}$ F, so $\beta = 3.7 \cdot 10^{-8}$. The best measured value of the equivalent temperature was $T_e = 1750$ K, against the expected value of 0.081 K. The reason why the expected equivalent temperature is so low is due to the fact that β is extremely low, so there is little back-action on the sphere and the thermodynamic temperature T would be barely increased. The fact that the measured T_e is much higher than expected, clearly shows that the mode was being excited by extra non-brownian noise.

5.2 The MiniGRAIL electronic box

The previous measurement also showed that the coupling β between the modes and the PZT is extremely small. To increase the β it is necessary to use a resonant capacitive transducer. Besides, to lower the electronic noise, a SQUID must also be used. So the necessity to build a read-out chain equal to that used by the Rome group. So the need for a new electronic box, built following the lines outlined during the design of the NAUTILUS read-out chain.

As for NAUTILUS, all the electronic components of the read-out chain are housed in a Cu OFHC box, plated with Sn40%Pb60%. Picture (5.5) shows the chamber that houses the decoupling capacitor and the polarization resistances. Since the MiniGRAIL rosette transducer has a capacity of the order of 1 nF, the decoupling capacitor is much smaller than that for NAUTILUS. Its capacity has been chosen to be of 15 nF. Again we used high- Q Teflon capacitors. The chamber that houses these components is quite small, so we could not use the usual polarization resistors. So, to build the redundant configuration of a serie of two parallels, we were forced to use tiny SMD resistors.

The superconducting transformer is quite similar to that of NAUTILUS. The holder has exactly the same dimensions and design, but the material is different: this time we used MACOR, a vitreous ceramic with a resistivity $\rho > 10^{16}\Omega/\text{cm}$. The number of turns per layer and the number of layers has been chosen in order to give an inductance of

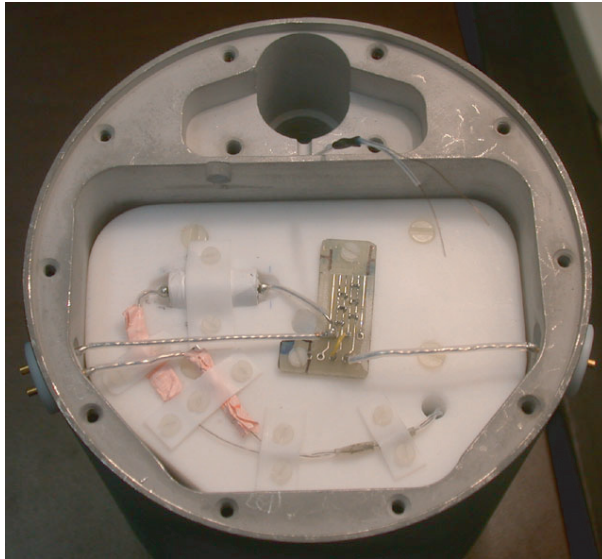


Figure 5.5: The electronic box for MiniGRAIL.

the primary coil of the order of 0.5 H at room temperature. Again we used Nb wire, 80 μm diameter, coated with FORMVAR[®]. The room temperature value¹ of L_0 is 0.55 H, while that at 4.2 K was 0.37 H.

We performed two Q measurements: one placing the transformer in the usual PVC box, shielded by Pb foils, and the other replacing the PVC box with a Cu box plated with Sn40%Pb60%. Both the measurements, done observing the free decay of the electrical mode, gave $Q \simeq 3 \cdot 10^5$.

We added two different secondary coils, one with a coupling coefficient of 0.4 and the other with $k \simeq 0.18$.

After connecting all the electronic components of the read-out chain,

¹Measured with the HP4192A LCR Meter.

we moved to Leiden, to perform the last Q measurement, that gave $Q = 1.8 \cdot 10^5$ with the decoupling capacitor and the polarization resistances connected to the circuit, and some SQUID measurements.

5.3 Measurements with single and double SQUID systems

These measurements turned out to be very important. This electronic box was meant to be connected to a two stage amplifier based on a DROS SQUID [73]. But when we connected this system to the secondary with $k = 0.4$, we saw that the SQUID was so unstable that could not lock at all. We then tried the secondary with $k = 0.18$. This time the SQUID was able to lock, even if the range of the parameters (bias current and modulation amplitude) was very narrow. Besides the measured noise was very high, of the order of $2 \cdot 10^{-5} \phi_0 / \sqrt{\text{Hz}}$, when the double SQUID noise is usually one order of magnitude lower.

So we decided to use a single Quantum Design SQUID, the same used on EXPLORER and NAUTILUS, connected to the $k = 0.4$ secondary coil. The result was that the SQUID could lock quite easily with a wide range of parameters, and the noise was lower by more than a factor of two. Figure (5.6) shows a part of the spectrum of the output signal of the SQUID. The large peak at the centre of the plot is a calibration signal, fed to the SQUID to monitor its gain and test its stability.

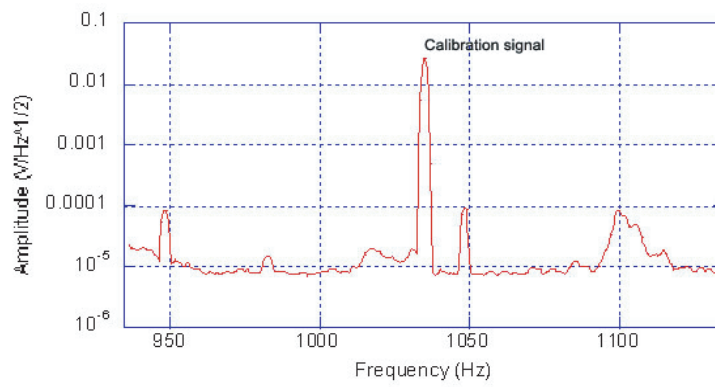


Figure 5.6: A part of the spectrum recorded with a single QD SQUID.

Chapter 6

Double SQUID system for the Rome detectors

In most practical applications the sensitivity of a SQUID with a standard modulation readout is usually good enough. There are, however, fundamental physics experiments, such as GW detectors, that require the highest possible sensitivity of a d.c. SQUID. In this case the standard readout may not be the best solution, because the overall sensitivity can be limited by the room-temperature preamplifier noise. Furthermore it can be seen [74] that the energy resolution of a single SQUID system is $\epsilon \simeq 3000\hbar$.

But it has been shown [73, 75, 76] that a double SQUID system can reach quantum limit energy resolution, as can be seen from figure (6.1). Besides, it has also been shown [77] that a double SQUID system can be

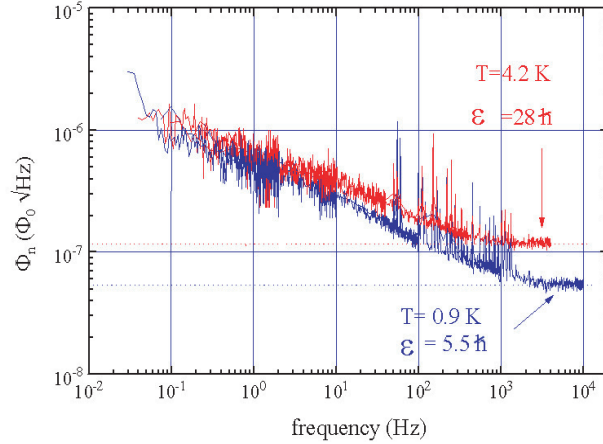


Figure 6.1: Experimental spectral noise density of the double SQUID system of Carelli *et al.*.

arranged in a stable configuration when connected to a high- Q resonant circuit.

So, the last part of the work of this thesis has been devoted to arrange the system of [75] in a configuration that can be used on one of the GW detectors of the Rome group.

The first SQUID (sensor) is made at the Institute of Photonic and Nanotechnologies of CNR, while the second SQUID is a commercial Quantum Design d.c. SQUID. We expect that when, connected to a high- Q resonant circuit, this system will show the typical instabilities of such systems, as those already observed on the Dutch double SQUID (see section 5.3). So that most of the work will be done on removing these effects.

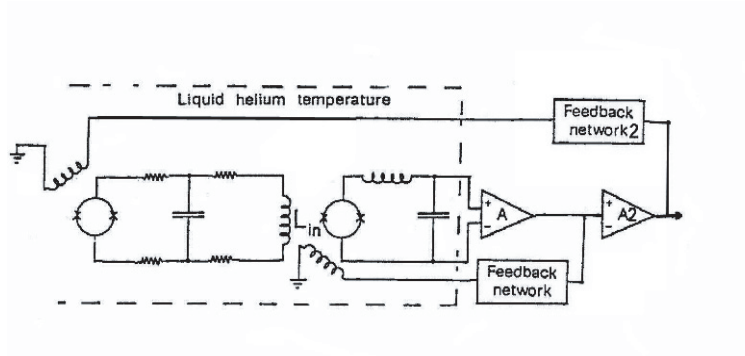


Figure 6.2: Scheme of the feedback networks of the double SQUID system.

6.1 First closed loop operation

The measurement reported in figure (6.1) was made with the sensor SQUID in open loop configuration. It means that no feedback was sent to the sensor SQUID to stabilize its working point. Instead, the Quantum Design SQUID was working in closed loop operation. Since this setup is not suitable for a GW detector, we built a feedback network to close the loop on the sensor SQUID. Figure (6.2) shows the scheme of the double SQUID feedback networks.

We acquired the $V - \phi$ characteristics for different bias currents (see figure (6.3)) to determine those with highest slope, so the best sensitivity. Then, we performed a noise measurement with this setup to see if the feedback network would introduce extra noise and if some unexpected instabilities would arise. The result of the measurement is reported in figure (6.4). No instability of the system was found. We were able to

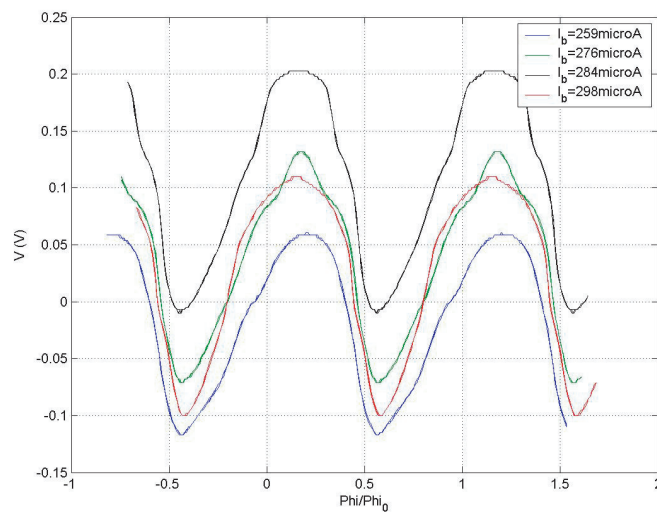


Figure 6.3: The $V - \phi$ characteristics for different bias currents. As can be seen the shape of the curves is very sensitive to I_b but the height of the curves is almost unaffected.

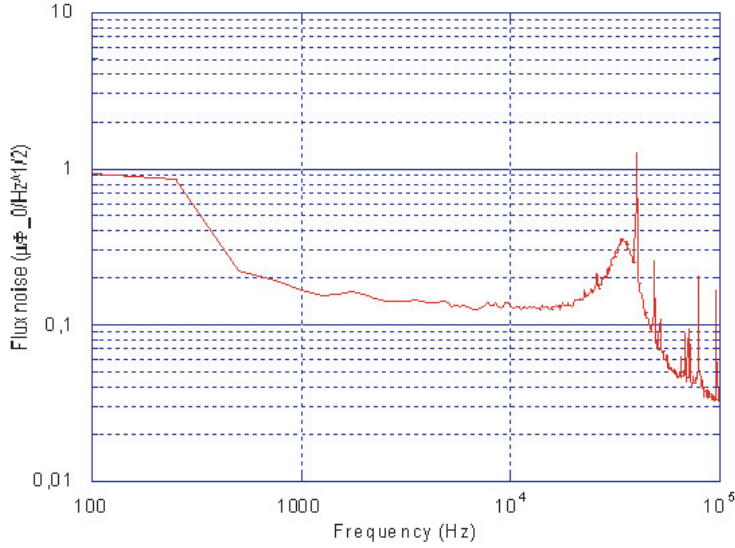


Figure 6.4: Measurement of the double SQUID noise in closed loop operation.

lock the whole system in a wide range of the parameters. This setup also allows us to choose the point, along the $V - \phi$ characteristics, where to lock the SQUID. Furthermore, as it can be seen from picture (6.4), the output noise spectrum is very clean and flat for a wide range of frequencies. The best noise result was $1.5 \cdot 10^{-7} \phi_0 / \sqrt{\text{Hz}}$ at 1 kHz and even lower at higher frequencies. This corresponds, roughly speaking, to an energy resolution of $\epsilon \simeq 30\hbar$.

We also explored different feedback setups, i.e. closing the loop on the sensor SQUID and keeping it open on the second, but the noise measurement were at least a factor of two worse and the selection of the working point was much more difficult.

These measurement have been performed keeping the input coil of the sensor SQUID open. But this is not a real setup, since when installed on a GW detector, the double SQUID system will be connected to a high- Q resonant circuit.

6.2 Characterization of the high- Q input circuit

The high- Q input circuit has been built following the indications given by the same work done for the NAUTILUS. At this time of the work, the absolute values of the inductances of the primary and secondary coils are of no importance. The inductance of the primary coil is 123 mH at room temperature and decreases to 96.7 mH at 4.2 K. The inductance of the secondary coil is 1 μ H at room temperature and 0.5 μ H at liquid helium temperature. The coupling coefficient is $k = 0.61$. Since this transformer has been equipped with two auxiliary coils of very low inductances, we also measured their coupling to the primary coil and found $k_1 = 0.03$ and $k_2 = 0.38$. These coils have been used as pick-up coils to perform the Q measurements.

Since our laboratory has been equipped with an acquisition system based on LabView¹, we were able to characterize the tranformer more deeply. We measured² the impedance of the primary coil from 10 Hz

¹See Appendix B for the diagram of the LabView VI.

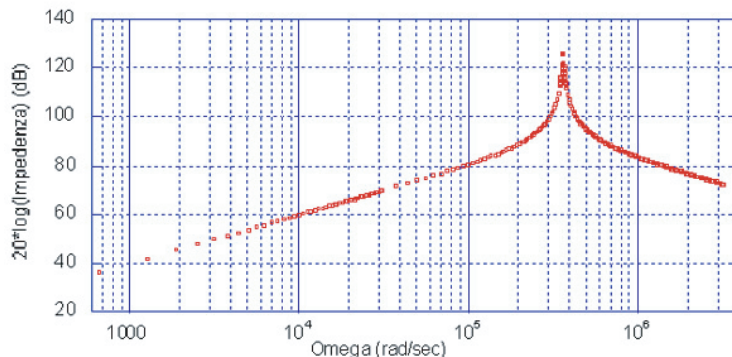


Figure 6.5: Bode plot of the inductance of the primary coil.

to 520 kHz. As can be seen from figure (6.5), the measurement shows that the primary coil behaves as an ideal inductor over a wide range of frequencies. The same measurement has been performed both on the secondary coil and on the high- Q Teflon capacitors, with the same results.

Then we performed several Q measurements, since it is important that this transformer is truly high- Q . The first measure was done by closing the inductance of the primary coil on the same capacitor used for the measurements for the NAUTILUS read-out chain. We observed the free decay of the electrical mode and obtained $Q = 8.6 \cdot 10^5$, which is high enough. We also verified that the value of Q does not depend on which auxiliary coil is used for the measurement. But since the inductance of the primary coil is very low, it turns out that the resonance frequency is very high, and it has been found to be $\nu_{el} = 5441$ Hz. This would be too far from the region of interest, that is around 1 kHz. So the only

²We acquired the output of the HP4192A LCR Meter via a GPIB 488.2 board.

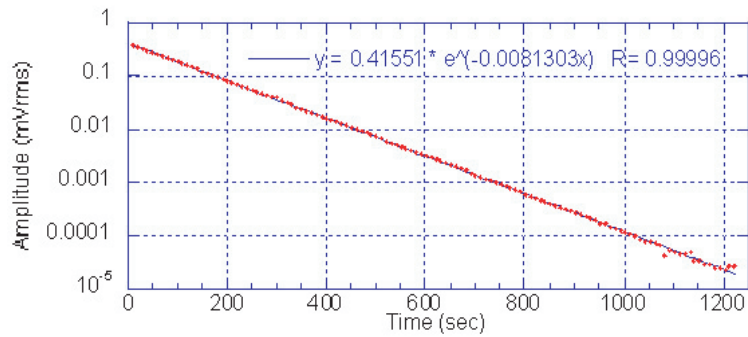


Figure 6.6: Decay of the electrical mode, data points are acquired every ten seconds.

way to decrease ν_{el} is to increase the value of the capacitance. We then used a capacitor with $C = 95.7 \text{ nF}$ at 4.2 K. But, unexpectedly, the Q was $2.2 \cdot 10^5$, lower by a factor of four with respect to the previous value. Fortunately we had another capacitor with high capacitance, $C = 86.9 \text{ nF}$ at 4.2 K. The result of the measurement is shown in figure (6.6). The resonance frequency is now $\nu_{el} = 1735 \text{ Hz}$ and the Q , obtained by fitting the data with an exponential decay, is $6.7 \cdot 10^5$.

Chapter 7

Conclusion

The main goal of this Ph.D. thesis was to develop the electronic part of the read-out chain for advanced GW detectors. The preliminary results obtained with NAUTILUS 2003, such as the increase by a factor of five of the detector's bandwidth and the decrease by more than a factor of two of the detector's noise temperature, clearly show that the work done is on the right way. We need to wait for the next year to have the results of the coincidence analysis and of the search for the pulsar remnant of supernova 1987A.

Results similar to that of NAUTILUS are expected from the Mini-GRAIL detector. It is easy to foresee a decrease of the noise temperature by at least a factor of 1000. Its next science run is scheduled to start by the end of this year.

On the other hand, it has been shown that it is possible to push the

noise of the first stage amplifier close to the quantum limits. At present, we are working to realize a new read-out chain based on a double SQUID amplifier to be implemented on the detectors of the Rome group.

Appendix A

A Matlab[©] code example

Here is the subroutine used to determine the inductance of the primary coil. The complete program is made of a number of other subroutines with a similar structure. The total length of the complete program is more than 2000 lines.

```
%code to calculate the inductance of the primary coil
%a=average radius; b=length; c=radial dimension;
%N=total number of windings;
%nb=number of windings on each layer;
%nc=number of layers; p=dimension of the wire.

disp('1)Calcolo dell induttanza del primario');
disp('2)Menu principale');
o=input('Scegliere ');
if o==1
rm=input('Inserisci il raggio minimo (cm) ');          %
b=input('Inserisci la lunghezza della bobina (cm) ');%
```

```

nc=input('Inserisci il numero di strati ');           %
p=input('Inserisci lo spessore del filo (um) ');     %
p1=p*1e-4;                                           %calculation of some
a=rm+p1*nc/2;                                       %equivalent parameters
c=p1*nc;                                             %
N=b*c/p1^2;                                         %
n=b/p1;                                             %
for i=1:nc                                          %
r(i)=rm+i*p1;                                       %
s(i)=2*pi*r(i)*n;                                    %
end                                                  %
m=sum(s);                                           %
load D1;                                           %loading some of the
load E1;                                           %Grover tables
load F1;                                           %
rho=c/b;                                           %more equivalent parameters
alfa=c/(2*a);                                       %
mu=1/rho;                                           %
nu=b/(2*a);                                         %
if rho<=1                                           %procedure to look into the
y=D1(:,1);                                         %Grover tables
x=D1(1,:);                                         %
f=y-rho;                                           %
d=x-alfa;                                          %
for i=2:22                                         %
for j=2:22                                         %
if rho==y(j) & alfa==x(i)%
k=D1(j,i);                                         %
else                                              %
if d(i-1)>-0.05 & d(i)<0.05 %first order Newton
if f(j-1)>-0.05 & f(j)<0.05 %linear interpolation
dx1=D1(j-1,i-1)-D1(j-1,i); %
dy1=D1(j-1,i-1)-D1(j,i-1); %
u=-d(i-1)/0.05;                                     %
v=-f(j-1)/0.05;                                     %

```

```

k=D1(j-1,i-1)-u*dx1-v*dy1; %
end %
end %
end %
end %
end %
if mu<=1 %
y=E1(:,1); %
x=E1(1,:); %
f=y-mu; %
d=x-alfa; %
for i=2:22 %
for j=2:22 %
if mu==y(j) & alfa==x(i) %
k=E1(j,i); %
else %
if d(i-1)>-0.05 & d(i)<0.05 %
if f(j-1)>-0.05 & f(j)<0.05 %
dx1=E1(j-1,i-1)-E1(j-1,i); %
dy1=E1(j-1,i-1)-E1(j,i-1); %
u=-d(i-1)/0.05; %
v=-f(j-1)/0.05; %
k=E1(j-1,i-1)-u*dx1-v*dy1; %
end %
end %
end %
end %
end %
z=F1(:,1); %
d=nu-z; %
for i=2:101 %
if nu==z(i) %
K=F1(i,2); %

```

```

else %
if d(i-1)<0.01 & d(i)>-0.01 %
dx1=F1(i-1,2)-F1(i,2); %
dx12=F1(i,2)-F1(i+1,2); %
dx2=dx1-dx12; %
u=d(i-1)/0.01; %
K=F1(i-1,2)-u*(dx1-(1-u)*dx2/2); %
end %
end %
end %
disp('La induttanza del primario in microH')
L=0.019739*2*a^2*N^2*(K-k)/b %inductance calculation
disp('Lunghezza del filo in Km') %quantity of needed wire
lung=m*1e-5 %
primario %
end %
if o==2
trasformer
end

```

Appendix B

LabView code example

Here we show both the Control Panel (figure (B.1)) and the Diagram (figure (B.2)) of the VI used to acquire the data used to characterize the circuit elements. The VI acquires and saves to a file the following parameters: $|Z|$, the phase θ , R , L , C and also the Q . The behaviour of these quantities versus frequency is displayed on-line.

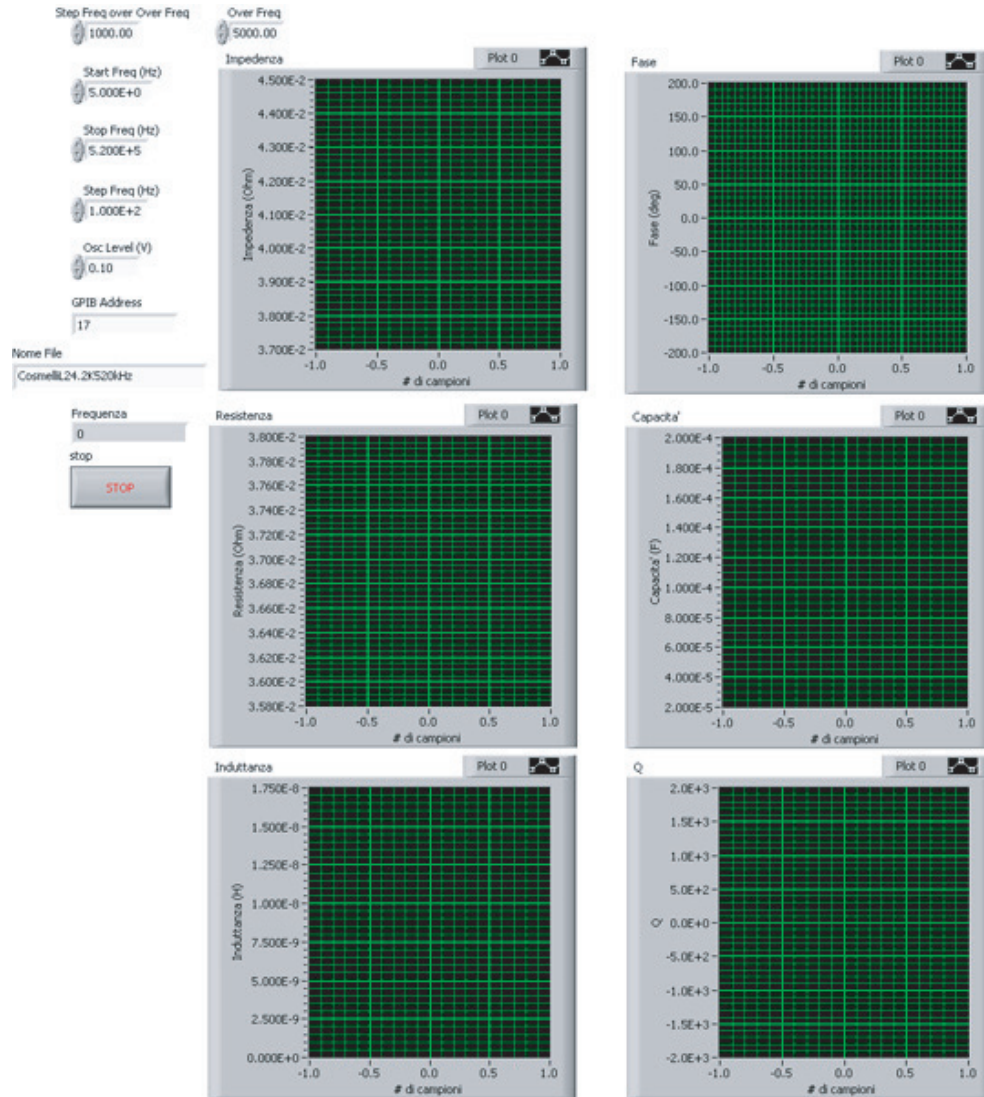


Figure B.1: The Control Panel of the LabView VI. It is possible to set the starting, stop and step frequency of the acquisition and the amplitude of the signal.

Bibliography

- [1] Landau-Lifšits, “*Teoria dei campi*”, Editori Riuniti.
- [2] K. S. Thorne, “*Gravitational Waves*”, *Proceedings of the Snowball 95 Summer Study on Particle and Nuclear Astrophysics and Cosmology*, ed. E. W. Kolb e R. Peccei (World Scientific, Singapore).
- [3] B. F. Schutz, *Class. Quantum Grav.* **16**, A131-A156 (1999).
- [4] Guido Pizzella, “*Fisica Sperimentale del Campo Gravitazionale*”, Edizioni NIS.
- [5] I.S. Heng *et al.*, *Class. Quantum Grav.* **19**, 1889-1895 (2002).
- [6] J.P. Zendri *et al.*, *Class. Quantum Grav.* **19**, 1991-1996 (2002)
- [7] P. Astone *et al.*, *Phys. Rev. Lett.* **91**, 11 (2003).
- [8] P. Astone *et al.*, *Class. Quantum Grav.* **19**, 1911-1917 (2002).
- [9] A. de Waard *et al.*, *Class. Quantum Grav.* **20**, S143-S151 (2003).
- [10] O.D. Aguiar *et al.*, *Braz. J. Phys.* **32**, 866-868 (2002).
- [11] R. E. Vogt, *The U.S. LIGO Project*, in “International Report LIGO”, pagg. 91-97, Caltech (USA) 1991.
- [12] F. Acernese *et al.*, *Class. Quantum Grav.* **20**, S609-S616 (2003).
- [13] M. Hewitson *et al.*, *Class. Quantum Grav.* **20**, S581-S591 (2003).

- [14] M. Ando *et al.*, *Class. Quantum Grav.* **19**, 1409-1412 (2002).
- [15] K.S. Thorne, in S.W. Hawking and W. Israel, editors, *Three Hundred Years of Gravitation*, pages 330-458. Cambridge University Press, 1987.
- [16] C. Kochanek, *Astrophys. J.*, 398:234, 1992.
- [17] P. Astone *et al.*, *Phys. Rev. D* **68**, 022001 (2003)
- [18] E. Amaldi, G. Pizzella, “*Teoria della Rivelazione delle Onde Gravitazionali*”, Corso della Scuola di Perfezionamento Dell’Università di Roma, 1976/77.
- [19] R. V. Wagoner e H. J. Paik, “*Proceedings of International Symposium of Experimental Gravitation, Pavia*” (Accademia Nazionale dei Lincei, Roma, 1976), pagg. 257-265.
- [20] M. Bianchi *et al.*, *Class. Quantum Grav.* **13**, 2865 (1996).
- [21] S. M. Merkowitz, W. Johnson, *Phys. Rev. D* **51**, 2546 (1995).
- [22] E. Coccia, J. A. Lobo e J. A. Ortega, *Phys. Rev. D* **52**, 3735 (1995).
- [23] J. Weber, *Phys. Rev.* **117**, 306 (1960).
- [24] R. P. Giffard, *Phys. Rev. D* **14**, 2478 (1976).
- [25] H. J. Paik, *J. of Appl. Phys.* **47**, 1168 (1976).
- [26] J-P. Richard, *Rev. Sci. Instrum.* **47**, 423 (1976).
- [27] P. Rapagnani, *Nuovo Cimento* **5C**, 385 (1982).
- [28] J-P. Richard, *Phys. Rev. Lett.* **521**, 165 (1984).
- [29] P. Astone, G. V. Pallottino and G. Pizzella, Internal Report LNF-96/001.
- [30] A. Papoulis “*Probability, random variables and stochastic processes*”, 2nd Ed. McGraw Hill, New York, 1984.

- [31] S. Johnson *et al.*, Nature **361**, 613 (1993).
- [32] R. L. Forward and D. Berman, Phys. Rev. Lett. **18**, 1071 (1967).
- [33] J. P. A. Clark and D. M. Eardly, Astrophys. J. **215**, 315 (1977).
- [34] D. Dewey, Phys. Rev. D **36**, 1577 (1987).
- [35] J. S. Bendat and A. G. Piersol, “*Measurement and analysis of random data*”, John Wiley & Sons, New York (1966).
- [36] P. F. Michelson, Mon. Not. R. Astr. Soc. **227**, 933 (1987).
- [37] E. Flanagan, Phys. Rev. D **48**, 2389 (1995).
- [38] P. Astone, J. A. Lobo and B. F. Shutz, Class. Quantum Grav. **11**, 2093 (1996).
- [39] Boughn *et al.*, Astrophys. J. **261**, L19 (1982).
- [40] P. Astone *et al.*, Phys. Rev. D **47**, 2 (1993).
- [41] W. W. Johnson *et al.*, “*Proceedings of the 1st Edoardo Amaldi Conference, Frascati 1994*”, E. Coccia, G. Pizzella, F. Ronga editors (World Scientific, Singapore, 1995).
- [42] E. Amaldi *et al.*, Astron. Astrophys. **216**, 325 (1989).
- [43] D. G. Blair *et al.*, Phys. Rev. Lett. **74**, 1908 (1995).
- [44] P. Astone *et al.*, Phys. Rev. D **47**, 10 (1993).
- [45] P. Astone *et al.*, Particles and Fields **50**, 21 (1991).
- [46] The dilution refrigerator has been designed and assembled in collaboration with Oxford Instruments Ltd.
- [47] M. Bassan, E. Coccia, I. Modena, G. Pizzella, P. Rapagnani, F. Ricci, “*Proceedings of the 5th Marcel Grossmann Meeting on General Relativity*”, Blair, Buckingham and Ruffini editors (World Scientific, London, 1989).

- [48] E. Coccia, V. Fafone, I. Modena, *Rev. Sci. Instr.* **63**, 5432 (1992).
- [49] M. Bassan, Y. Minenkov, R. Simonetti, “*Proceedings of the VIRGO Conference*”, F. Fidecaro and I. Ciufolini editors (World Scientific, Singapore, 1997).
- [50] E. Iarocci, *Nucl. Instr. and Meth.* **217**, 30 (1983).
- [51] E. Amaldi, G. Pizzella, *Nuovo Cimento* **C9**, 2 (1986).
- [52] F. Ricci, *Nucl. Instr. and Meth.* **A260**, 491 (1987).
- [53] J. Chiang, P. Michelson and J. Price, *Nucl. Instr. and Meth.* **A311**, 603 (1992).
- [54] P. Astone *et al.*, *Phys. Rev. Lett.* **84**, 14-17 (2000).
- [55] P. Astone *et al.*, *Astropart. Phys.* **7**, 231 (1997).
- [56] P. Astone *et al.*, *Class. Quantum Grav.* **19**, 5449-5463 (2002).
- [57] Z. A. Allen *et al.*, *Phys. Rev. Lett.* **85**, 5046 (2000).
- [58] J. Middleditch *et al.*, *New Astronomy* **5**, 243 (2000).
- [59] S. Nagataki and K. Sato, *Prog. Theor. Phys.* **105**, 429 (2001).
- [60] M. Bassan and G. Pizzella, Internal Report LNF-95/064(P).
- [61] J. P. Zendri *et al.*, “*Proceedings of the First Edoardo Amaldi Conference on Gravitational Waves Experiments*”, E. Coccia, G. Pizzella and F. Ronga editors (World Scientific, London, 1994).
- [62] M. Bassan, “*The GASP numerical model for resonant antennas*”, unpublished.
- [63] F. W. Grover, “*Inductance Calculations, working formulas and tables*”, D. Van Nostrand Company, Inc.
- [64] C. Hilbert and J. Clarke, *J. Low Temp. Phys.* **61**, 237 (1985).

- [65] P. Falferi *et al.*, Appl. Phys. Lett. **71**, 956 (1997).
- [66] R. P. Feynman, “*La Fisica di Feynman vol. 5: un seminario sulla superconduttività*”, Addison Wesley, London 1969.
- [67] A. Barone, G. Paternó, “*Physics and Applications of the Josephson effect*”, John Wiley and Sons, New York 1978.
- [68] J. Clarke, “*Superconducting Quantum Interference Devices for low frequency measurements*”, reprinted by “*Superconductor Applications: SQUIDS and Machines*”, Plenum Publ. Corp., New York 1977.
- [69] C. D. Tesche, J. Clarke, “*Proc. of the Applied Superconductivity Conference*”, Stanford 1976.
- [70] J. Clarke, W. M. Goubau, M. B. Ketchen, Jour. of Low Temp. Phys. **25**, N. 1/2, 1976.
- [71] E. Amaldi *et al.*, Lett. al Nuovo Cim. **18**, 425 (1977).
- [72] J. P. Richard, Phys. Rev. Lett. **52**, 165 (1984).
- [73] M. Podt, M. J. van Duuren, A. W. Hamster, J. Flokstra and H. Rogalla, Appl. Phys. Lett. **75**, 2316 (1999).
- [74] P. Falferi, M. Bonaldi, M. Cerdonio, M. Mück, A. Vinante, G. A. Prodi and S. Vitale, J. Low Temp. Phys. **123**, 275 (2001).
- [75] P. Carelli *et al.*, Appl. Phys. Lett. **72**, (1998).
- [76] P. Falferi *et al.*, Appl. Phys. Lett. **82**, 931 (2003).
- [77] A. Vinante *et al.*, Appl. Phys. Lett. **79**, 2597-2599 (2001).